JOURNAL OF GEOPHYSICAL RESEARCH, VOL. 106, NO. B8, PAGES 16,101-16,117, AUGUST 10, 2001

Three-dimensional shallow crustal emplacement at the 9°03'N overlapping spreading center on the East Pacific Rise: Correlations between magnetization and tomographic images

S. Bazin,[1,2] A. J. Harding,[1] G. M. Kent,[1] J. A. Orcutt,[1] C. H. Tong,[3] J. W. Pye,[3]
S. C. Singh,[2,3] P. J. Barton,[3] M. C. Sinha,[3,4] R. S. White,[3] R. W. Hobbs,[3]
and H. J. A. Van Avendonk[5]

Abstract. We report a three-dimensional (3-D) seismic reflection and tomographic survey conducted at the 9°03'N overlapping spreading center (OSC) on the East Pacific Rise to understand crustal accretion at this feature. Inversions of travel time data from 19 ocean bottom hydrophones provide a 3-D image of the shallow velocity structure beneath the nontransform offset and associated discordance zone. Seismic analysis indicates that layer 2A thickness varies between 100 and 900 m and averages 430 m throughout the study area. The heterogeneous upper crustal structure at the OSC region contrasts with the simpler symmetric structure flanking the midsegments of the East Pacific Rise. The crust affected by the OSC migration carries evidence for the complex accretion at the axial discontinuity where the overlap basin may act as a lava pond. An area of thick layer 2A covers the southern half of the overlap basin and the propagating ridge tip and shows good correlation with a high magnetization region. Comparison of the magnetic field anomaly derived from the seismic structure model with the observed sea surface magnetic anomaly suggests that a significant portion of the high magnetization can be related to magnetic source thickness variation rather than solely to the geochemistry of the volcanic rocks.

1. Introduction

Seismic layer 2A is generally interpreted as corresponding to the extrusive rocks in the volcanic structure of the oceanic crust, although there is not universal agreement on this identification [e.g., *Houtz and Ewing*, 1976; *Rohr*, 1994]. The geometry of layer 2A has been studied intensively in the last decade, and seismic experiments using different methods have been successful in mapping the velocity and thickness of layer 2A in various spreading rate regimes: at the fast spreading East Pacific Rise (EPR) [*Toomey et al.*, 1990, 1994; *Harding et al.*, 1993; *Kent et al.*, 1994; *Carbotte et al.*, 1997; S. Hussenoeder et al., Fine-scale seismic structure of young upper crust on the fast spreading East Pacific Rise, submitted to *Journal of Geophysical Research*, 2001, hereinafter referred to as Hussenoeder et al., submitted manuscript, 2001], the intermediate Juan de Fuca Ridge [*Rohr et al.*, 1988; *Cudrak and Clowes*, 1993; *McDonald et al.*, 1994], the slow spreading Mid-Atlantic Ridge [*Barclay et al.*, 1998], and Reykjanes Ridge [*Smallwood and White*, 1998]. Prior surveys, however, have focused predominantly on midsegments of the rise axis, and the structure of layer 2A remains largely unknown in complicated geometries such as ridge segment ends. Investigating different accretion environments provides insight into layer 2A processes and helps to test competing ideas about its relationship to lithology and tectonic processes such as faulting and hydrothermal circulation. With this motivation we present here the results of a joint seismic and magnetic study of the three-dimensional structure of layer 2A at an overlapping spreading center (OSC) on the EPR. A more detailed tomographic analysis will be presented elsewhere (C. H. Tong et al., Three-dimensional shallow crustal emplacement at the 9°03'N overlapping spreading center on the East Pacific Rise: Tomographic imaging and axial magma chamber reflectors, hereinafter referred to as Tong et al., manuscript in preparation, 2001).

The objective of the 1997 Anatomy of a Ridge Axis Discontinuity (ARAD) survey was to image the three-dimensional structure of an axial discontinuity. A multichannel seismic (MCS) survey was centered on the 9°03'N OSC and a broader refraction/tomography experiment extended 30 km on either side of the EPR. This study is part of a more complete investigation including the nature of the axial melt lens [*Kent et al.*, 2000] and the extent of its underlying low velocity zone and crustal thickness [*Bazin*, 2000]. In this study, we investigate the regional geometry of layer 2A using velocity models obtained by the refraction/tomography experiment. The air gun/ocean bottom receiver technique provides detailed information on upper crustal velocities owing to the combination of high source repetition rate and broad coverage.

Earlier investigations identified regions of high magnetization associated with the propagating limb of OSCs, which were

---

[1] Cecil H. and Ida M. Green Institute of Geophysics and Planetary Physics, Scripps Institution of Oceanography, University of California, San Diego, La Jolla, California.

[2] Now at Laboratoire de Géosciences Marines, Institut de Physique du Globe de Paris, Paris, France.

[3] Bullard Laboratories, Department of Earth Sciences, University of Cambridge, Cambridge, England, United Kingdom.

[4] Now at School of Ocean and Earth Science, University of Southampton, Southampton, England, United Kingdom.

[5] Department of Geology and Geophysics, University of Wyoming, Laramie, Wyoming.

Paper number 2001JB000371.
0148-0227/01/2001JB000371$09.00

attributed to highly fractionated, highly magnetized lavas [*Sempéré et al.*, 1984; *Sempéré*, 1991; *Carbotte and Macdonald*, 1992]. We take advantage of a new seismic model of overlapping spreading centers to examine the origin of the anomalous magnetic signal at these features. The magnetic field anomaly is generated by the magnetized upper oceanic crust, and seismic layer 2A is certainly related to the magnetic source layer [*Tivey and Johnson*, 1993; *Tivey*, 1994; *Schouten et al.*, 1999]. Short-wavelength variations of the oceanic magnetic field result from a combination of two factors, thickness of the magnetic source layer and the magnetization intensity of the rocks. By removing the thickness component from the magnetic anomaly signature we can map the magnetization intensity of the basalts in the OSC region. For the first time, documented extrusive thickness (this study), melt lens geometry and depth [*Kent et al.*, 2000; Tong et al., manuscript in preparation, 2001], geochemical sampling [*Natland et al.*, 1986; *Langmuir et al.*, 1986], magnetization data [this study; *Sempéré et al.*, 1984; *Carbotte and Macdonald*, 1992], and geomorphologic studies [*Sempéré and Macdonald*, 1986] are available for the same area. We seize the opportunity to address the relationships between these observations.

2. Geologic Setting

The 9°03′N OSC is the only major discontinuity along the 9°N EPR ridge segment bounded to the north by the Clipperton fracture zone (FZ) at 10°10′N and to the south by the Siqueiros FZ at 8°20′N. This OSC is associated with an off-axis discordant zone marking its trace: A V-shaped wake of pseudofaults extends from the present-day OSC at 9°03′N back to 1 Ma. The orientation of its trail indicates that the discontinuity has been episodically migrating southward along the rise crest [e.g., *Lonsdale*, 1985; *Carbotte and Macdonald*, 1992; *Macdonald et al.*, 1992]. The OSC migration has averaged 42 mm/yr since anomaly 2 time, but its rate and kinematic pattern have not been steady; periods of rapid and slow propagation as well an episode of northward propagation have occurred. In the kinematic model for this OSC, *Carbotte and Macdonald* [1992] describe two types of progression. In the first type, the propagating limb lengthens until it joins the other ridge limb, letting the entire overlap basin and opposite limb raft outward. In the second type, inward jumping of one of the rift tips (also called ridge tip self-decapitation) causes the abandonment of a short section of axial ridge, leaving the overlap basin intact. As a result, the western discordant zone consists of a series of abandoned ridge tips 2–40 km long, 200–400 m higher than the deep wake and fossil overlap basins, while the one on the eastern flank is restricted to a broad wake of anomalous bathymetry, 100–300 m deeper than surrounding seafloor. Relict overlap basins indicate that the size of the offset has increased during its southern migration. The two rift zones now overlap by 27 km, are 8 km apart, and are separated by a 500-m-deep elliptical basin (Figure 1). The offset is right stepping, with the eastern ridge axis propagating into undisturbed crust. The sediment cover observed by deep-towed images reveals that the eastern propagating ridge tip has experienced recent volcanic episodes while the western tip exhibits older lavas on average (relative age of 1.2–2.2 on a 1–4 scale inferred from sediment cover [*Sempéré and Macdonald*, 1986]). A narrow band of fresh pillow basalts is present on the highly fissured crest of the propagating limb. The two limbs reach similar depths, but the eastern limb widens toward its southern end at the expense of the overlap basin (see Plate 2 of *Sempéré and Macdonald* [1986]).

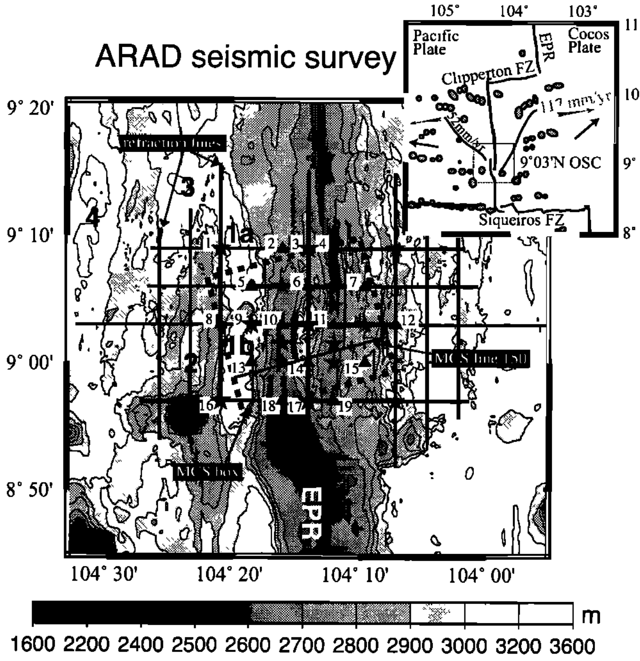

Figure 1. Bathymetric map of the 9°03′N OSC displaying refraction shot lines and instrument locations. The 19 instruments used in the tomography inversion are annotated by solid symbols and are numbered. Triangles designate Scripps L-Cheapo hydrophones and stars designate Cambridge mini-DOBSs. The 201 MCS lines were shot in a 20 by 20 km^2 box delineated by dashed box. We outlined MCS line 150 as it is discussed in the text. The 1a, 1b, 2, 3, and 4 labels indicate relict basins as numbered by *Carbotte and Macdonald* [1992]. Inset shows the survey site relative to the 9°N segment and the OSC discordance zone. Rates and directions of the seafloor spreading (shaded arrows) and of OSC migration (V-shaped lines) are from *Carbotte and Macdonald* [1992], while the seamount distribution (stippled circles) is from *Macdonald et al.* [1992]. The orientations of the Cocos and Pacific plate motions with respect to the hot spot reference frame are shown by solid arrows [*Gripp and Gordon*, 1990].

The ARAD three-dimensional (3-D) reflectivity survey revealed the intricate geometry of the axial melt lens at the OSC location. A strong axial magma chamber (AMC) reflector underlies both limbs and the northern part of the overlap basin [*Kent at al.*, 2000]. The eastern limb AMC, 4 km wide to the north of the overlap, narrows significantly toward the south and finally plunges by several hundreds of meters before disappearing. The detailed three-dimensional reflectivity data reveal that the eastern melt sill is fed, at least partly, through pathways of magma emerging from beneath the overlap basin. In contrast, the AMC on the western limb has a width more typical of the EPR [e.g., *Phipps Morgan et al.*, 1994]. However, the western melt lens is not crest centered but is shifted toward the eastern side of the ridge.

Petrologic sampling along the 9°N segment revealed a geochemical segmentation, which correlates with the general morphology of the ridge axis [*Langmuir et al.*, 1986]. The 9°N segment encompasses numerous small discontinuities ranging from kinks in the axial summit trough [*Haymon et al.*, 1991; *Fornari et al.*, 1998] to deviations from axial linearity (DEVALs

[*Langmuir et al.*, 1986]), and small nonoverlapping offsets (SNOOs [*Batiza and Margolis*, 1986]). The correspondence between axial discontinuities and the geochemical segmentation suggests that morphological and magmatic segmentations of the ridge crest are related. In addition, lavas sampled at the 9°03′N OSC have markedly different geochemical properties: Enriched and normal (N-type) basalts are found on the western limb, while N-type ferroandesites and dacites are present on the eastern limb [*Natland et al.*, 1986]. The eastern limb is associated with highly evolved basalts enriched in iron and titanium oxides that have low Mg numbers (Mg # = Mg/(Mg + Fe^{2+})). Highly fractionated basalts are frequently found in association with rift propagation and have been attributed to isolated melt bodies [*Sinton et al.*, 1983; *Langmuir et al.*, 1986].

3. Seismic Modeling

The ARAD seismic survey was a joint experiment between the Scripps Institution of Oceanography, the British Institutions Reflection Profiling Syndicate, and the University of Cambridge. The survey was conducted aboard the R/V *Maurice Ewing* in the fall of 1997. An array of 30 ocean bottom seismometers and hydrophones (OBSs and OBHs) was deployed, and of these, 19 instruments had sufficient data quality for this analysis (Figure 1). The seismic source was a tuned 10-gun array with a total volume of 50 L (3050 cubic inches). Eleven refraction lines (2000 shots total, along 28- to 72-km length profiles) were shot with sources fired every 110 s to limit reverberation noise (~250 m shot interval along tracks); seven lines were shot along and four lines were shot across the ridge axis. A dense MCS survey was conducted in a 20 by 20 km box with edges oriented 345°–075°. The analysis of the 11 refraction shot lines and a subset of the MCS shots is presented in this study. We completed the seismic analysis by performing preliminary 2-D forward modeling, 3-D ray-tracing, and tomographic inversions. Descriptions of data quality and data reduction are found in Appendix A.

3.1. Preliminary 2-D Modeling

Seismic tomography is typically not an ideal tool for resolving the velocity gradient of layer 2A because in conventional marine data, seismic energy turning in the upper part of the crust is hidden by the high-amplitude water wave. Compared to most wide-angle data with sea surface shots, the fine spacing of the ARAD MCS shots (~38 m shot spacing along tracks versus the more typical 250 m) provides better constraints on the velocity structure in the upper crust. Indeed, the low shot interval of the ARAD data produces more information on the layer 2A branch of the travel time curve (~6.5 more data points). Since the range window in which the layer 2A branch begins before the layer 2B branch is very narrow (window depending on crustal velocities and water depth), the shot interval is an important consideration.

The triplication from the base of layer 2A provides a basis for measuring the surficial velocity and thickness of layer 2A (Plate 1a). The travel time curves were forward modeled to obtain a depth-velocity model at site 7, located 3 km to the east of the ridge axis at water depth of 2.8 km (Plate 1b). Visual comparisons of the record section for OBH 7 and the modeled travel time curve were used to iteratively improve the velocity model and the data fit. As a result, we estimated the surficial velocity (2.6 km/s) and thickness of the layer (400 m) in the vicinity of the instrument (parameters comparable with those obtained by waveform analysis of expanding spread profile (ESP) data recorded off-axis at 9°35′N [*Vera et al.*, 1990]). The profile from site 7 was taken as the starting velocity model for the 3-D tomographic analysis.

3.2. Three-Dimensional Tomographic Inversion

Three-dimensional seismic tomography provides a means for investigating the complex magmatic and tectonic processes which form and modify the oceanic crust. We analyze the travel time data by three-dimensional ray tracing and iterative, nonlinear tomographic inversion [*Van Avendonk*, 1998; *Van Avendonk et al.*, 1998]. The ray-tracing method is an adaptation of the shortest path [*Moser*, 1991] and ray-bending methods [*Moser et al.*, 1992]. Rough topography is included through the use of sheared grid cells in which the velocity grid parallels the ocean floor topography [*Toomey et al.*, 1994]. This hybrid technique is used to efficiently calculate first arrival travel times through a 3-D velocity grid. The initial 3-D grid is constructed with the starting 1-D velocity model of Plate 1b. The rough topography of the area has a large effect on the ray entry points, and so a detailed bathymetric grid is necessary for the forward ray-tracing step. The entry point for each source-receiver pair is calculated iteratively as part of the ray-bending calculation and is not constrained to the 2-D plane containing the source and receiver.

The inversion of the travel time residuals is performed with least squares penalties on the data misfit and on a measure of model roughness defined in terms of horizontal and vertical velocity gradients scaled by appropriate lengths [*Toomey et al.*, 1994; *Van Avendonk et al.*, 1998]. The vertical smoothing length scales are predefined by the gradients in the initial velocity-depth profile. The horizontal length scales are chosen a-priori to be larger than the vertical length scales in order to conform to the expectation of predominantly horizontal structures in the Earth. Horizontal smoothing length scales must increase with depth to match the corresponding increase in vertical scales. The model domain is 60 km across axis by 40 km along axis. The horizontal grid spacing is 600 m while the vertical spacing gradually increases from 100 m at the seafloor to 500 m at the greater model depths.

Over 20,000 refracted arrivals (*Pg* phase from all the refraction shots and near MCS shots) are included in our tomographic inversion. In order to improve the vertical resolution at shallow depths we do not weight arrival time picks solely with respect to the accuracy of the picking [*Toomey et al.*, 1990, 1994; *Sohn et al.*, 1997; *Barclay et al.*, 1998; *Van Avendonk et al.*, 1998] but follow *Zhang and Toksöz* [1998] and weight the travel time data with respect to their range in order to fit preferentially the less numerous rays turning in the shallow crust.

3.3. Seismic Results

The initial travel time residuals attest to the presence of a heterogeneous upper crust. Residuals for a subset of the travel time data with ranges shorter than 8 km are presented in Figure 2. The residuals are assigned near the shot locations, and we removed the appropriate average receiver delay from each residual. Therefore we can assume that the residual delays are mostly caused by uppermost crustal heterogeneities near the shot locations [*McDonald et al.*, 1994]. Positive residuals are observed at the eastern ridge tip and the relict basins,

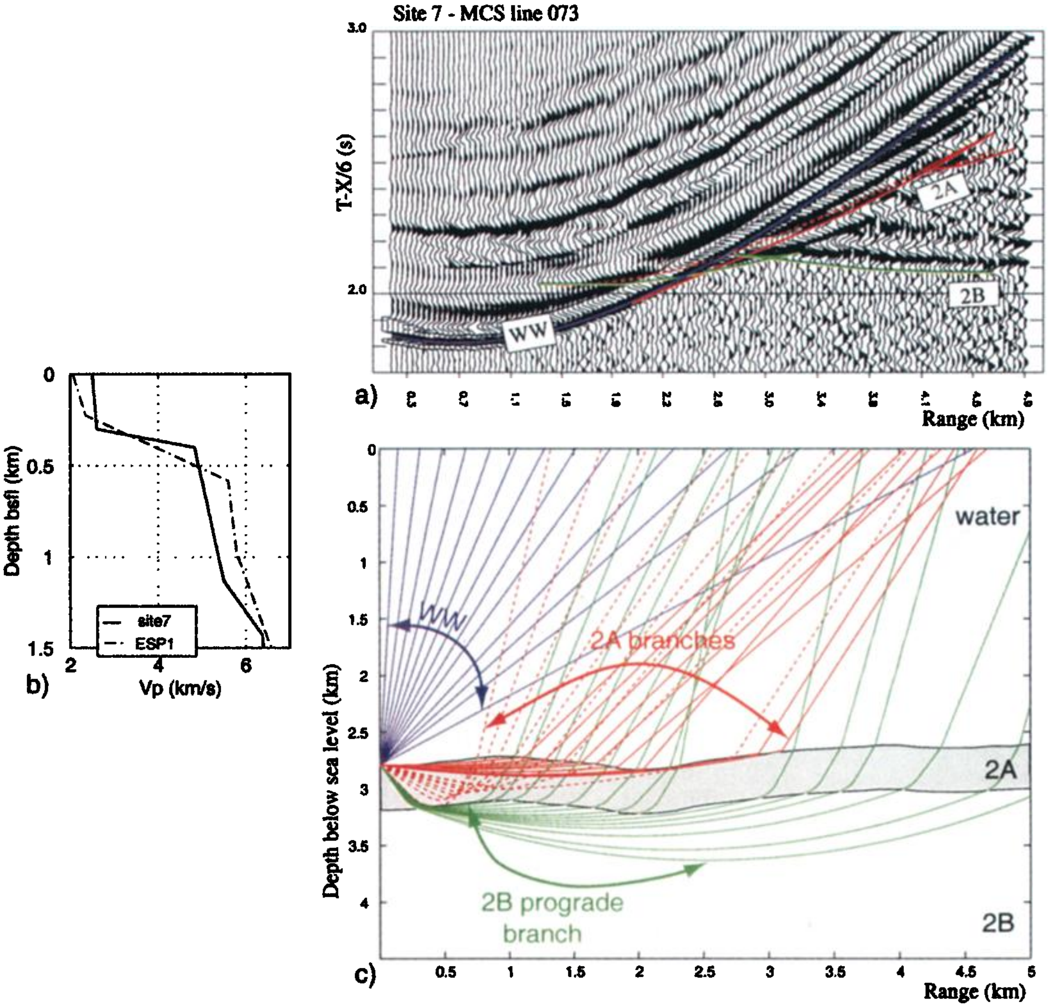

Plate 1. (a) A record section from the instrument located at site 7. Data have been reduced to 6 km/s and band-pass-filtered between 5 and 20 Hz. A variable amplitude scale is used in order to emphasize weaker arrivals beyond the water wave. A trial-and-error modification of a simple model was performed to match the main branches observed in the data. The colored curves (water wave in blue, layer 2A branch in red, and layer 2B branch in green) represent the travel times generated by 2-D ray tracing. The red dashed line represents the layer 2A retrograde branch in the triplication. (b) Velocity-depth profiles. For comparison, the dashed velocity-depth model was obtained by expanding spread profile 1 (ESP1) acquired 10 km east of the rise axis at 9°35′N by *Vera et al.* [1990]. Site 7 is located 3 km east of the rise axis. (c) Ray paths computed with the velocity-depth of Plate 1b for shots at the sea surface and a receiver on the seafloor (rays color-coded as in Plate 1a).

implying lower velocities or thicker layer 2A. The smallest residuals are observed at site 7 where we estimated the starting depth-velocity model. The complete range of travel time delay is 0.3 s (delays varying from −0.122 to +0.185 s, when compared to the initial 1-D model of Plate 1b) with an average close to zero.

In order to avoid undue influence of deep rays on the upper crustal velocity structure the tomographic inversion was performed in two steps, starting with a subset of the travel time picks. When including only rays <12 km range, the initial RMS travel time residual was 121 ms. After 6 iterations the RMS residual decreased to 23 ms (normalized variance reduction of 96%). After this step, most of the shallow velocity structure is resolved; however, the ray coverage is not uniform, and we improve it by incorporating additional picks. During a second suite of iterations (8 iterations), including the whole set of *Pg* picks (short and long ranges), the RMS travel time residual started at 124 ms and was reduced to 25 ms (additional normalized variance reduction of 97%). A better fitting model could be obtained, but the model would yield rougher velocity anomalies more likely associated with noise than velocity. Most of the data have picking errors of <12 ms, yet picking errors up to 24 ms are included in the inversion. Possible sources of errors associated with the data collection include uncertainties in the instrument clock drifts (~3 ms), in the bathymetry grid (10 m uncertainty), in the shot locations (3 m uncertainty in vertical and 5 m in horizontal directions), and in the instrument locations (7.7 ms resulting from uncertainty in instrument x-y position and 4.4 ms from uncertainty in instrument depth). The accuracy of the ray tracing is also a source of error (5 ms resulting from uncertainty in travel time computation [*Van Avendonk et al.*, 2001] and 5 ms uncertainty in ray-entry point estimate) affecting the predicted RMS misfit (17 ms total). Higher ray-tracing accuracy could be obtained with a finer velocity grid; however, we chose to limit the 3-D grid size to 600 m for computational efficiency. The chosen final level of data fit is thus possibly slightly conservative: ~25 ms for the model versus an estimated 17 ms for the data error.

The best fitting average model is shown in Figure 3, where it is compared with profiles obtained from other experiments in the same area. Although slightly slower than previous results, our mean velocity profile contains velocity gradients comparable to those estimated by other methods (ESP [*Vera et al.*, 1990] and 2-D refraction lines [*Christeson et al.*, 1997]). Some gradient reduction is to be expected because of the influence of the smoothing constraints. Velocities within layer 3 and the bottom of layer 2B (below 1 km depth) match previous estimates. The upper part of layer 2B appears slower on average than for the previous results. We believe, however, that this velocity reduction is a consequence of the smoothing inherent in our inversion method combined with the averaging procedure. Indeed, at the same depth, some layer 2B velocities are averaged with layer 2A velocities. Longitudinal and transverse transects through the velocity grid are presented in Figures 4 and 5, respectively. The upper crustal velocity structure appears highly variable: Variations in upper seismic layer thickness are observed on sections running parallel to the rise axis including along the relict basins, the present overlap basin, and the eastern ridge limb. In contrast, the upper crust appears uniform on the western ridge limb and the eastern flank (Figure 4). Three rise-perpendicular vertical sections (Figure 5) show that in addition to the pattern of layer 2A thickening away from the ridge axis, low-velocity regions occur within the OSC basin, and the two relict basins located west of the EPR. Unfortunately, we were unable to map significant variations in seafloor velocity, as our travel time inversion uses only layer 2A travel times occurring outside the water wave.

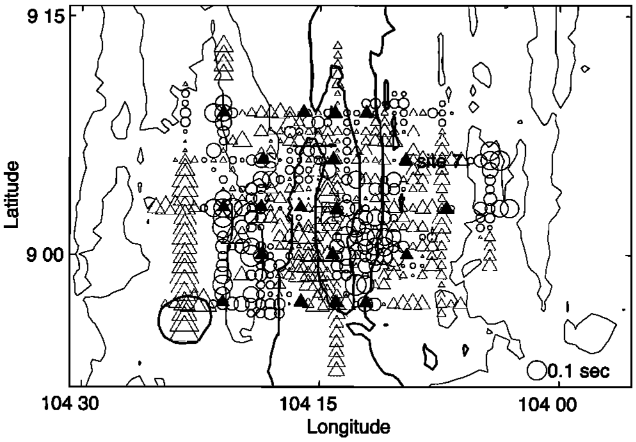

Figure 2. Distribution of the initial travel time residuals calculated with the velocity model shown in Plate 1b. Triangles show fast residuals, while circles show slow ones. The symbols are located at the shot positions, and their sizes represent the magnitude of the residuals. A −0.1-s residual is shown for reference. The residuals are averaged for shots within 0.5 km radius, and each residual value is adjusted for the average receiver residual of the appropriate instrument. This approach removes the bias that occurs if an instrument is located in an anomalous region. The heavy solid line is the 2700-m isobath contouring the two OSC limbs; the thin solid line is the 3000-m isobath contouring the relict basins 1a and 1b on the Pacific side.

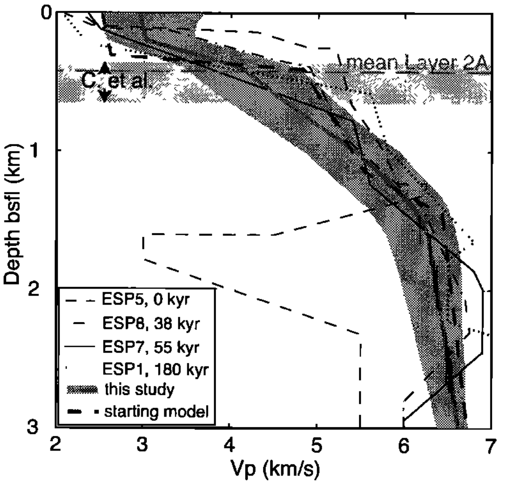

Figure 3. Comparision between compressional velocity-depth models. The shaded line shows the inversion average result of this study. Solid lines present different velocity profiles obtained with expanding spread profile data recorded at 9°35′N, on axis (ESP5), 2.1 km east of the axis (ESP8), 3.1 km west (ESP7), and 10 km east (ESP1) [*Vera et al.*, 1990]. The shaded area bounding our average profile represents the minimum and maximum velocities computed from our final 3-D velocity grid by along-axis averaging (approximately simulating the ESP's geometry). The light shaded window represents the range of layer 2A thickness estimates (varying between 360 and 660 m) from a two-dimensional analysis at 9°35′N [*Christeson et al.*, 1997]. The dashed shaded line is our starting velocity model.

We wish to map the variability of layer 2A thickness in the study area. Tomographic methods can resolve lateral velocity variations, yet the velocity gradient information is limited due to smoothing constraints and the sole use of delay times without amplitude analysis. The final 3-D velocity models presented in this paper are highly smoothed, so that it is not possible to use breaks in the velocity gradients to delimit seismic layers. We seek a definition of layer 2A that is as compatible as possible to that which would be derived from MCS data. On the MCS reflection data collected during the ARAD survey a discontinuous but strong reflection is observed ~0.2–0.4 s below the seafloor reflection. This event is attributed to the base of layer 2A [e.g., *Harding et al.*, 1993; *Carbotte et al.*, 1997]. Figure 6 shows two-way travel times (TWTT) to the base of layer 2A picked along a representative stacked common depth point (CDP) profile running across the OSC. Integrated vertical travel times to the 4 or 4.5 km/s isovelocity horizon in our 3-D final velocity model match the layer 2A reflections. MCS picks manifest short-wavelength variations which are not resolvable by tomography because of the large station spacing (~5 km) and the coarse grid cells. However, the long wavelength travel time signal is similar for the two seismic methods. We applied this approach to 10 MCS profiles. TWTTs and times estimated with the 3-D velocity grid show general agreement, although layer 2A reflections are not observed on CDP gathers where layer 2A is unusually thick (i.e., deeper isovelocity contours). Accordingly, we use the 4 km/s velocity contour as a proxy to define the boundary between layer 2A and layer 2B and expand this delineation to the whole 3-D velocity

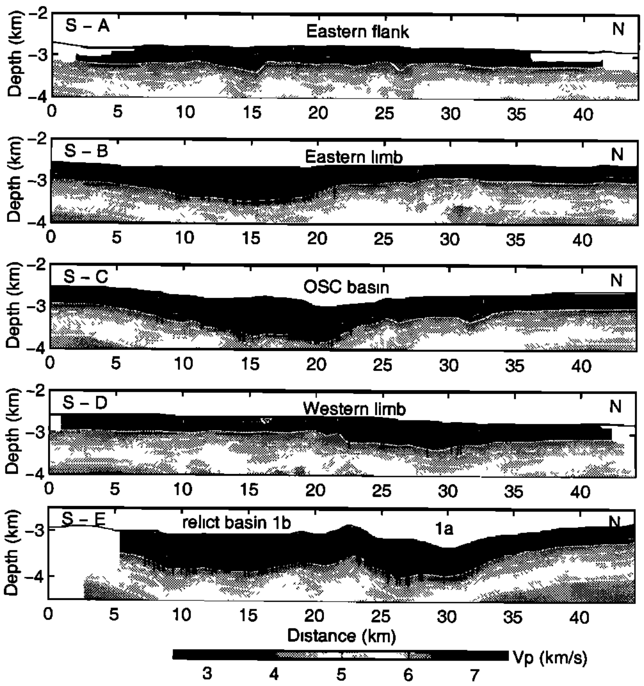

Figure 4. Rise-parallel slices through the velocity model illustrate the variability of the upper crustal structure. Isovelocity contours at 3, 4, 5, and 6 km/s are in white, while those for 3.5, 4.5, and 5.5 km/s are in dashed white. Velocities are shaded where ray coverage exists. The five panels display along-axis profiles that step progressively westward (see red transects in Plate 2). Transect A presents a slice through the Cocos side crust; the upper crust is quite uniform. Transect B illustrates a slice of the propagating limb; layer 2A thickens toward the ridge tip. Transect C shows thick layer 2A in the southern half of the overlap basin. Transect D reveals a thin and uniform layer 2A on the western rise axis. Transect E runs through the relict basins 1a and 1b; layer 2A thickness is almost double that on the Cocos side at a similar distance from the rise axis.

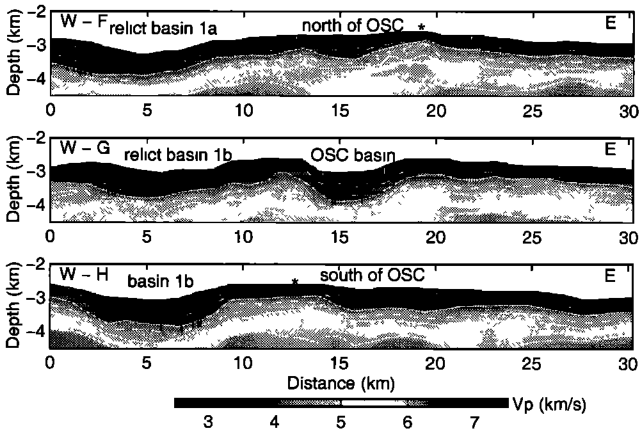

Figure 5. Rise-perpendicular slices through the velocity model (see blue transects in Plate 2). Transect G shows a profile running across the OSC. Transects F and H present the structure north and south of the OSC. Layer 2A is the thinnest at the eastern rise crest in transect F and at the western rise crest in transect H (areas marked by asterisks). In addition to the pattern of layer 2A thickening away from these two crestal areas, unusually thick layer 2A zones occur in the overlap basin and the relict basins located west of the EPR axis.

grid. Further support for our definition of layer 2A as the crustal section above the 4 km/s contour is the observation that much of the spatial variation in upper crustal velocity structure apparent in Figures 4 and 5 occurs above this velocity contour. It appears that choosing 4.5 or 5 km/s isovelocities would not significantly change the long-wavelength thickness variations; however, the resulting average thickness would be greater.

The resulting thickness map for seismic layer 2A is shown in Plate 2. Layer 2A thickness varies significantly laterally; it averages between 300 and 500 m (430 m mean), but in some areas it is >800 m thick. The observed delays at the propagating limb, the overlap basins, and the relict basins (Figure 2) result from thick layer 2A. Layer 2A is thin (100–200 m) on the ridge crest (southern half of the western limb crest and northern half of the eastern limb crest) and thickens toward the flanks, as generally observed across the EPR [*Harding et al.*, 1993; *Toomey et al.*, 1990, 1994; *Carbotte et al.*, 1997; Hussenoeder et al., submitted manuscript, 2001]. Within the present overlap region the most noticeable feature is a zone of thick layer 2A (over 800 m thick) where the eastern limb broadens and forms a flat plateau. This thick region coincides with positive travel time delays in the initial model as illustrated in Figure 2. Specifically, the data recorded by site 14 manifest a delay of 0.2 s between the east and the west side of the instrument (Plate 3a). This delay can be explained if layer 2A was ~600 m thicker to the east than west of the receiver. Plate 2b illustrates the corresponding ray diagram; the upper crust is well sampled by the dense ray paths emerging from the MCS shots.

Outside of the present overlap basin, areas of thick layer 2A occur exclusively in the western discordant zone and seem to correlate with the distribution of relict overlap basins and ridge tips. Figure 7 summarizes the areas of thick layer 2A as detected by the tomographic inversion. On the west flank, we observe zones of thick layer 2A located in the relict basins 1a, 1b, and less clearly in basin 3 (basins numbered according to the convention of *Carbotte and Macdonald* [1992]). Basin 3 is outside the MCS box and instrument array, and so its upper crust is not as well constrained by the tomographic inversion and the estimated layer 2A thickness, although greater than average, does not reach 650 m. However, we observe slow delays for the few rays that intersect basin 3 (Figure 2), and

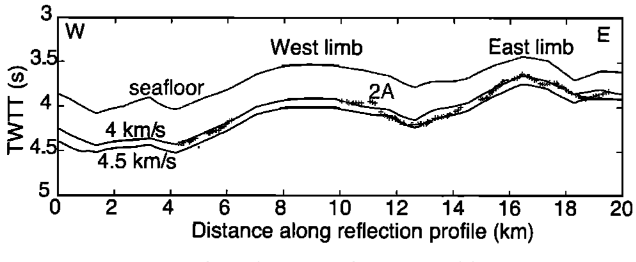

Figure 6. Comparison between layer 2A thickness from tomographic inversions and from MCS reflections. We picked layer 2A event (two-way travel times displayed by pluses) along a stacked common depth point (CDP) profile running across the OSC (location of CDP profile indicated in Plate 2). Travel times to the seafloor along the profile and integrated vertical travel times for two isovelocity contours extracted from our final velocity grid (4.0 and 4.5 km/s) are also shown. Notice that layer 2A reflections lie generally between the 4.0 and 4.5 km/s isovelocity contours.

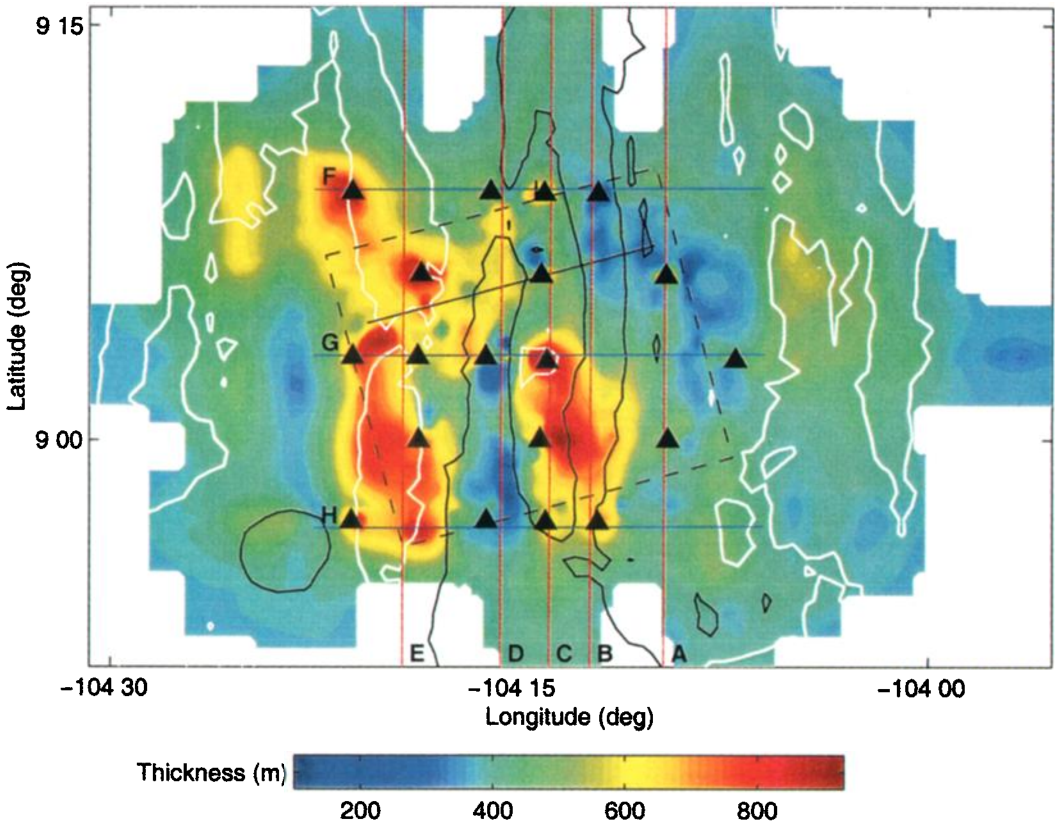

Plate 2. Map view of the 3-D velocity structure obtained from the delay time inversion. Depth to the 4 km/s isovelocity contour is used as proxy for layer 2A thickness. Layer 2A thickness averages 430 m in the study area. The layer is thinnest on the rise crest, while thick areas are centered on the propagating ridge tip, the southern half of the overlap basin, and the relict basins. Bathymetric contours are overlain for reference; black and white contours are 2700 and 3000 m isobaths, respectively. Triangles designate the 19 instruments used for the tomographic inversion. The dashed line shows the extent of the MCS box. The continuous black line shows the location the CDP profile used to illustrate the calibration of our velocity model for layer 2A thickness estimates (see Figure 6). The red lines show the locations of the five rise-parallel transects of Figure 4, and the blue lines show the locations of the three rise-perpendicular transects of Figure 5.

preliminary results from a recent refraction experiment running through this relict basin confirm our sparse observations [*Canales et al.*, 1999].

A travel time signal associated with the relict basins was identified in a 1993 seismic experiment north of the OSC [*Christeson et al.*, 1997]. The southernmost line of that survey intersects the older relict basins 3 and 4. To explain the large delays recorded by two OBSs, Christeson et al. preferred lower layer 2B/3 velocities to a thicker layer 2 given that the maximum variability of layer 2 thickness in the area was 300 m. With the insight from our new data set we propose that the delays in the distant relict basins might also originate from some layer 2A lateral thickness variations. We hypothesize from the observed thickness distribution that regions of thick layer 2A are a consistent feature of relict basins.

3.4. Seismic Resolution Analysis

A simple, though by no means complete, evaluation of the resolution of the three-dimensional imaging can be obtained from the distribution of seismic ray paths. A contour map representing the derivative weight sum (DWS [*Toomey et al.*, 1994]) distribution is shown in Figure 8. The DWS can be taken as a measure of the density of seismic rays influencing each model parameter and therefore outlines the general ray coverage. Unfortunately, several seismic instruments deployed on the Cocos plate did not produce data, so the ray sampling on the east flank is not as dense as on the west flank of the ridge axis and in the basin.

One can also assess the degree to which the tomographic model accurately reproduces the structure of the OSC by performing three-dimensional resolution tests. With synthetic inversions we can test whether the size and amplitude of the thick layer 2A areas present in the tomographic model are resolvable with the available data coverage. We evaluate the model resolution by reconstructing a known velocity anomaly with the same ray geometry as used for the tomographic inversion. A collection of 12 low-velocity anomalies is placed in the upper crust at 350 m below the seafloor (Plate 4). Anomalies placed in the center of the model box are well recovered both in terms of velocity and thickness variations, and little lateral smearing is apparent. Anomalies placed within the ray-covered area, but outside the instrument layout, are only partially resolved. As the ray density is lower on the eastern flank, the imaging resolution is poorer in this area. However, this test shows that the ray sampling would have been sufficient to recover velocity anomalies on the east flank similar in size to those detected on the west flank, as far as 10 km east from the

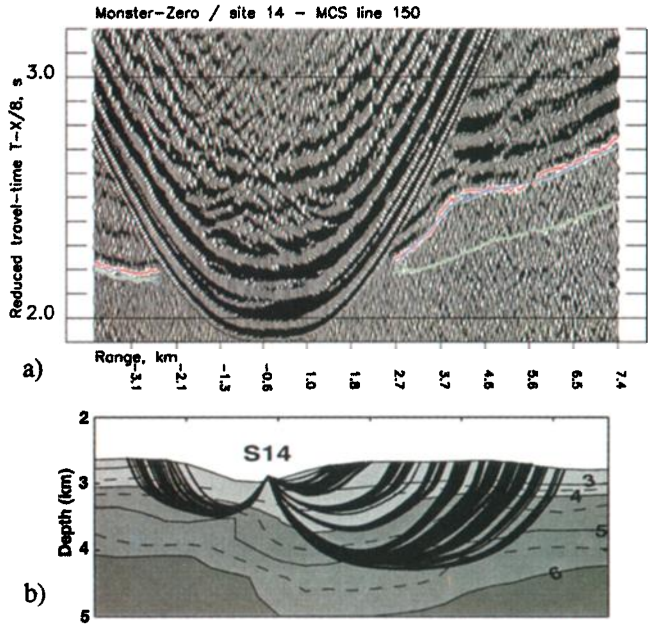

Plate 3. (a) Representative record section illustrating the layer 2A travel time signal observed with the dense MCS shots. The data were recorded at site 14 along MCS shot line 150 (track line location in Figure 1), reduced to 8 km/s and band-pass-filtered between 5 and 20 Hz. The data picks are in red, while the travel times calculated through the initial 1-D velocity model are in green. This initial model fits the data to the west of the instrument but the modeled travel times are 0.2 s too fast on the east side. This delay can be explained if layer 2A is ~600 m thicker (average velocity 3 km/s × 0.2 s delay) to the east of the instrument. The blue curve shows the data fit through the final velocity grid. (b) Ray paths corresponding to the blue travel time curve. Topography along the shot line and contours from the final velocity model are also shown: 3, 4, 5, and 6 km/s isovelocity contours are displayed as black lines, while 3.5, 4.5, and 5.5 km/s contours are displayed as dashed lines.

rise axis. The resolution tests demonstrate that we are able to resolve a velocity anomaly of similar amplitude (30% slower) and size (few kilometers in diameter) to the thick layer 2A zones mapped in this study. Therefore the upper crustal velocity structure within the OSC area can be considered to be well constrained.

4. Magnetic Modeling

The discordance zones of OSCs are generally characterized by a broad wake of deep bathymetry and high magnetic field anomalies [e.g., *Lonsdale*, 1983; *Macdonald et al.*, 1992]. The positive magnetic anomaly associated with the present location of the 9°03'N OSC can be seen in Plate 5a. We conducted a three-dimensional magnetic inversion of the dense sea surface magnetic data collected in the area (using an ambient field declination of 8.2°, inclination 30.6°, and assuming a geocentric dipole with zero declination and 17.6° inclination for the magnetization). Magnetic data were only gathered during one third of the ARAD survey (the gray box in Plate 5a outlines the coverage), as the magnetometer interfered with air gun and streamer operation. Outside the ARAD coverage, we incorporated a 1-km spaced data grid [*Carbotte and Macdonald*, 1992]. We used the Fourier inversion technique developed by *Parker and Huestis* [1974] as updated by *Macdonald et al.* [1980], which includes the effect of the topography and the phase shift due to latitude and ridge axis orientation. We solved for the apparent crustal magnetization distribution for a constant 430-m-thick source layer with the upper bound defined by the topography; the resultant solution is shown in Plate 5b. The magnetization

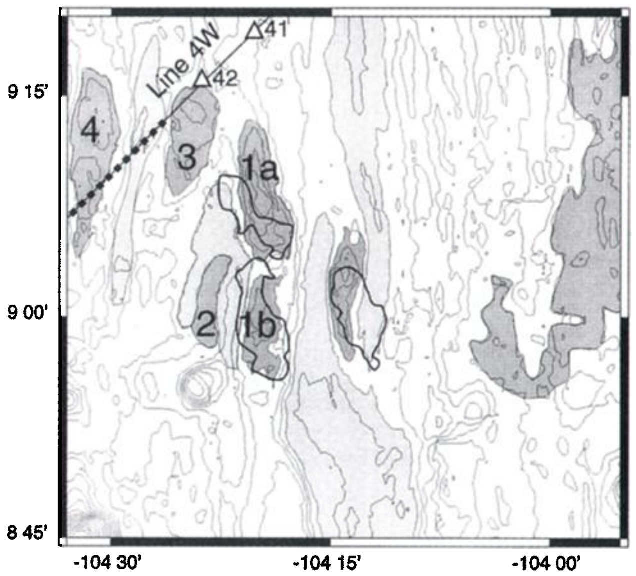

Figure 7. Bathymetry map of the OSC and discordant zone. Shallow regions, including rise axis and relict overlap ridge tips are delineated in light shading. Relict basins are delineated in dark shading and are numbered as by *Carbotte and Macdonald* [1992]. Anomalously thick seismic layer 2A (thickness ≥650 m) found by this study are outlined in heavy black contours. We observe three regions of thick layer 2A associated with the present overlap basin, with relict basins 1a and 1b, and possibly with relict basin 3 (however, the thickness does not reach 650 m). The region of slow seismic velocities, discussed in the *Christeson et al.* [1997] analysis, is shown as dashes along their line 4W.

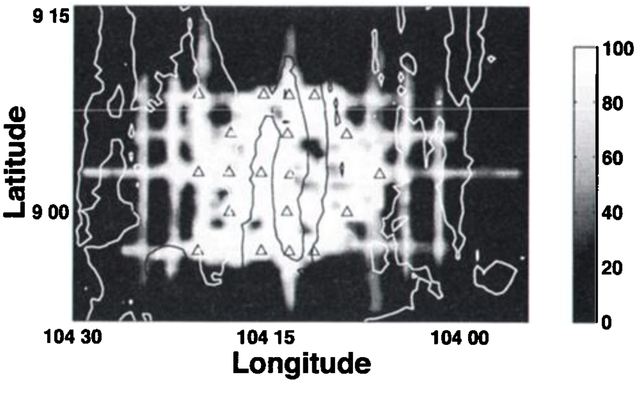

Figure 8. Contour map of the spatially averaged derivative weight sum (DWS) is shown for a depth of 0.5 km below seafloor. The DWS is the sum of the Frechet matrix elements for one model parameter in the inversion scheme. The normalized DWS represents an approximation of the relative ray density and of the data sensitivity in the model. Triangles show the locations of the 19 instruments used. The 2700- and 3000-m isobaths are shown in black and white, respectively, for reference.

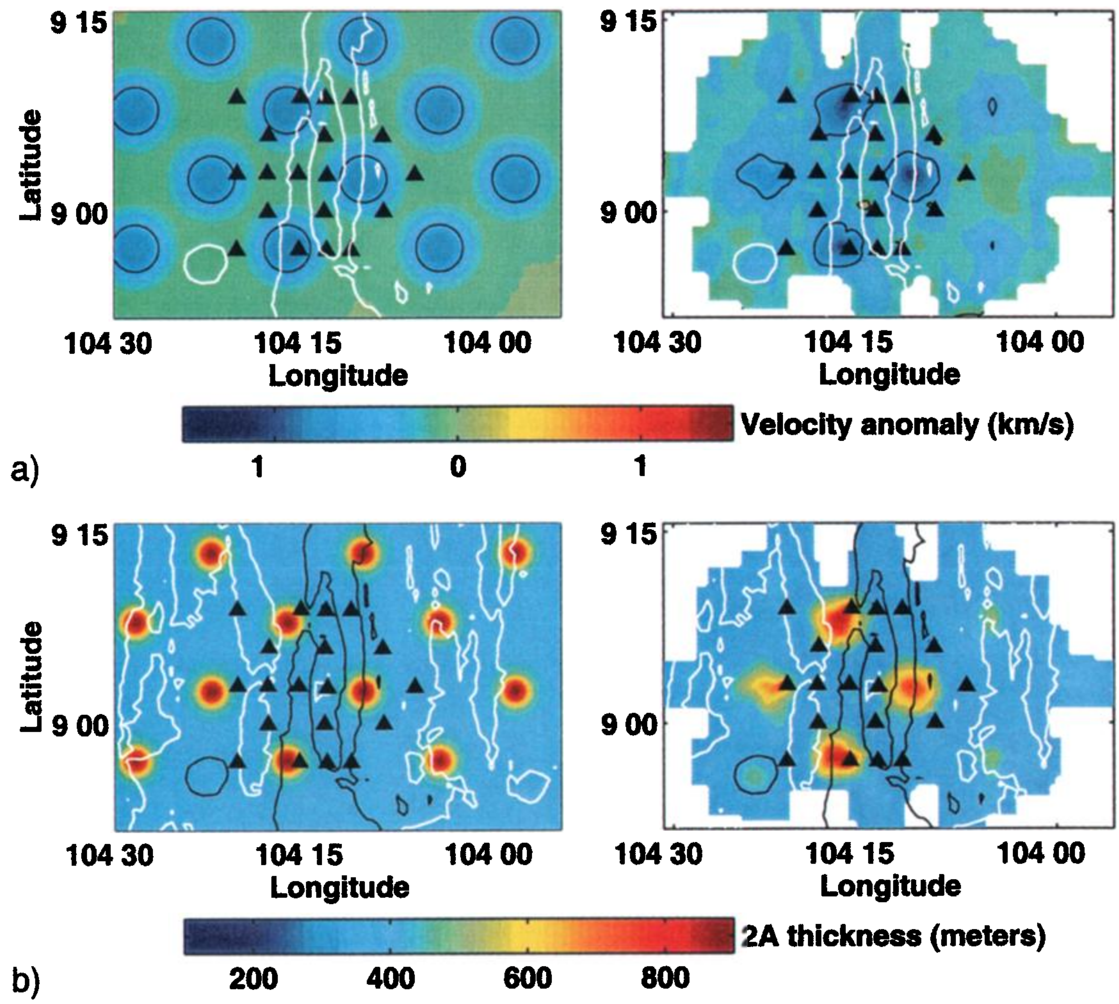

Plate 4. Resolution test. (a) (left) A map view of 12 velocity anomalies (circular Gaussian anomalies of 30% lower velocities) used for the test. The 3-D velocity model is extracted at 350 m below the seafloor. (right) The recovered anomalies at the same depth using the same shot-receiver geometry as in the tomographic inversion and with a similar travel time residual. The colored areas show the extent of the ray coverage. The black lines contour the velocity anomalies of 0 and −1 km/s. Triangles show the locations of the 19 instruments used. The 2700-m isobath (white contour) is overlain for reference. (b) (left) A map view of the tested layer 2A geometry (430 m layer with peaks to 900 m thickness). (right) The recovered thickness for the anomalies (same 4 km/s isovelocity contour as the one used in real case).

was assumed to be in the same direction as the geocentric dipole (0° declination, 17.6° inclination). A band-pass cosine taper filter with short-wavelength cutoff from 4 to 8 km and a long-wavelength cutoff of 400–800 km was applied to the magnetization grid at each step of the inversion to assure convergence. We computed the magnetization distribution using lower cutoff wavelengths, but 4 km gave the lowest RMS misfit for the recalculated anomaly field (32 nT); no annihilator was added to the solution. As observed previously by *Sempéré et al.* [1984] and *Carbotte and Macdonald* [1992], the anomalous magnetic field associated with the OSC is not attributable to the effect of bathymetric relief alone; a large component comes from the existence of a pronounced magnetization high at the propagating limb. *Sempéré et al.* [1984] pointed out that in order to obtain such variations by magnetized source layer thickness alone, a thickness increase by a factor of 2 to 3 was required. They thought such thickening was improbable at the spreading axis and favored an increase in crustal magnetization.

The extrusives are likely to be the main source for magnetic anomalies in young crust [*Talwani et al.*, 1971]. Indeed, we observe a positive correlation between the area of thick seismic layer 2A at the eastern ridge tip and overlap basin and the high values of computed magnetization (Plates 5b and 5c). To investigate this association, we modeled the magnetic anomaly generated by a constant source magnetization (25 A/m based on typical natural remanence measurements at the EPR [e.g., *Gee and Kent*, 1998]) and a magnetized layer with variable thickness [*Blakely*, 1995] inferred from the seismic layer 2A pattern. The anomaly at the propagating ridge tip is partially recovered by the variable source layer (Plate 5d), but outside of the dipole signal generated by the thick zone at the ridge tip, the fit of the sea surface data is now poor (144 nT RMS misfit). We conclude that additional factors contribute to the magnetic

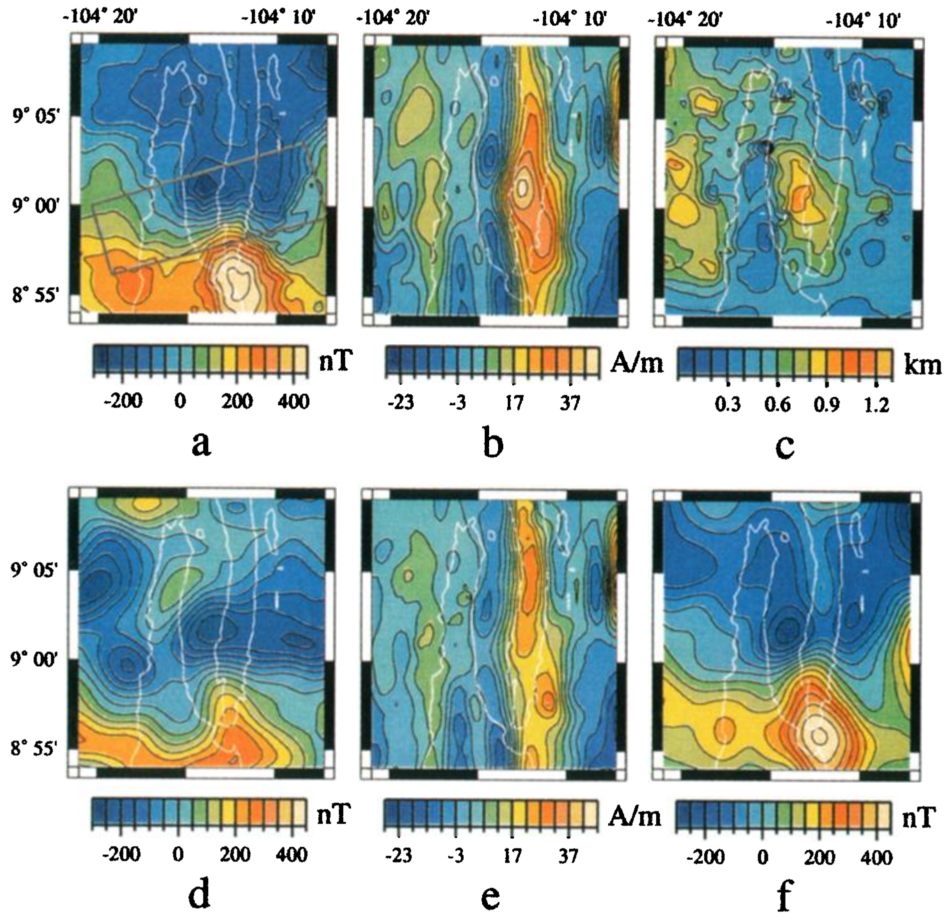

Plate 5. (a) Sea surface magnetic field anomaly. The new magnetic data acquired during the ARAD survey are outlined by the gray box. The 2700-m isobath contouring the ridge axis is overlain for reference (white contour). (b) Magnetization solution from 3-D inversion assuming a 430-m-thick magnetized layer. A magnetization high is centered on the propagating limb. (c) Layer 2A thickness variations. The thickness pattern seems to correlate with the magnetization solution of Plate 5b. (d) Magnetic anomaly model generated by the observed seismic layer 2A geometry with a constant magnetization (25 A/m). A significant portion of the high magnetization at the eastern ridge tip may be related to source thickness variation, but additional factors must contribute to the anomaly. (e) Magnetization distribution from which the source layer thickness contribution has been removed. The propagating limb is still more magnetized than the retreating one, and a narrow band of intense magnetization is now centered on the eastern rise crest. (f) Magnetic anomaly model generated by the observed seismic layer 2A thickness with the scaled magnetization distribution of Plate 5e. The recovered magnetic field matches the main features of the sea surface magnetic anomaly of Plate 5a.

field signal observed in the area. Short-wavelength magnetic anomaly variations result from variations in the magnetization intensity of the basalts, in the geometry of the magnetic source layer, and in the direction of magnetization. Which of these variables dominates the magnetic signal remains controversial [*Tivey and Johnson*, 1993; *Tivey*, 1994; *Gee et al.*, 1996; *Lee et al.*, 1996; *Schouten et al.*, 1999].

In order to quantify the relative contributions that magnetization intensity and source layer variations make to the magnetic field anomaly collected in the OSC area, we removed the effect generated by the geometry of the source layer. Because the magnetic inversion accounts for the effects of topographic and geometric skewness (ridge orientation and latitude), it is relatively straightforward to modify the inversion solution for nonuniform layer thickness. Comparison of inversion solutions for constant thickness layers indicates that doubling the thickness (0.5–1 km) results in sea-surface anomaly amplitudes 176% higher. We used the quasi-linearity between source thickness and magnetization intensity to investigate the magnetic intensity distribution at the OSC assuming that the seismically determined layer 2A acts as the magnetic source layer. Good correspondence has previously been observed between seismic layer 2A thickness and magnetization distribution on young oceanic crust [*Tivey and Johnson*, 1993; *Tivey*, 1994] and a technique that scales magnetization distribution with layer 2A thickness has been successfully applied along the Reykjanes Ridge [*Smallwood and White*, 1998]. Our magnetization solution scaled for the variable source layer is shown in Plate 5e. If seismic layer 2A coincides with the magnetic source layer, then our scaled magnetization solution should now only reflect variations in magnetization intensity of the basalts. Our new magnetization distribution with the geometry that corresponds to layer 2A generates a magnetic anomaly that matches all the main features of the observed anomaly data with a RMS misfit of 55 nT (Plate 5f). Considering the nonuniqueness in our inversion solution, the magnitudes predicted by our scaled magnetization solution cannot be exactly quantified. However, the good fit of the recalculated field gives some confidence in the inferred pattern. In our refined magnetization intensity distribution the propagating ridge still has higher values than the surrounding seafloor, but the local high is reduced to a narrow feature centered on the northern half of the eastern ridge crest.

5. Discussion

5.1. Origins and Interpretations of Seismic Layer 2A

From early investigations of oceanic crust, analogies have been made between the observed seismic layers and the layered petrology of ophiolite complexes [e.g., *Nicolas*, 1989], but the agreement between lithologic and seismic structures is still an unresolved issue. The debate originates in part from the misleading impression given by the use of the term "seismic layers." The analysis of refraction data yielded an early formalization of an oceanic seismic model: *Raitt* [1963] originally proposed a simplified crustal structure composed of two uniform velocity layers, layers 2 and 3 (layer 1 represented sediment deposits). This seismic layering was, in part, imposed by the data analysis applied at the time and was not required by the travel time data. A further subdivision of seismic layer 2 into homogeneous layers 2A and 2B [*Houtz and Ewing*, 1976] was followed by the construction of more accurate and continuous depth-velocity profiles [*Kennett and Orcutt*, 1976; *Spudich and Orcutt*, 1980]. Despite its descriptive limitations, the terminology of the "stair-stepped" seismic layers has remained. At the same time, laboratory measurements on ophiolite rocks demonstrated that sample velocities are in good agreement with oceanic crustal refraction velocities [e.g., *Christensen and Salisbury*, 1975; *Christensen*, 1978; *Spudich and Orcutt*, 1980]. Furthermore, layer thicknesses observed in ophiolites and thicknesses derived from oceanic seismic models were comparable [e.g., *Nicolas*, 1989]; seismic layer 2 would correspond to pillow lavas and sheeted dikes of the ophiolite sequence, and layer 3 would correspond to the gabbro unit, comprising isotropic and cumulate intrusives. Submersible observations of normal EPR-type crust, exposed on the walls of Hess Deep rift also yielded extrusive layer thicknesses comparable to that derived from seismic models [*Francheteau et al.*, 1992]. Inspite of a general resemblance between seismic and lithological layering, comparisons of lithostratigraphic drilling logs and depth-velocity models rule out a straightforward universal correspondence. Indeed, a refraction study in the vicinity of Deep Sea Drilling Project Hole 504B indicates that the base of seismic layer 2 lies within the sheeted dike complex [*Detrick et al.*, 1994]. Nevertheless, the small number of deep penetration drill holes coupled with the inherent differences in resolution of the geophysical methods and drilling logs limits the extent to which the relationship between the two can be investigated. For example, seismic layering and lithologic layering may not coincide vertically at a single drill hole, but their lateral variations may correspond such that there is a well-defined relationship between lithologic and seismic layering.

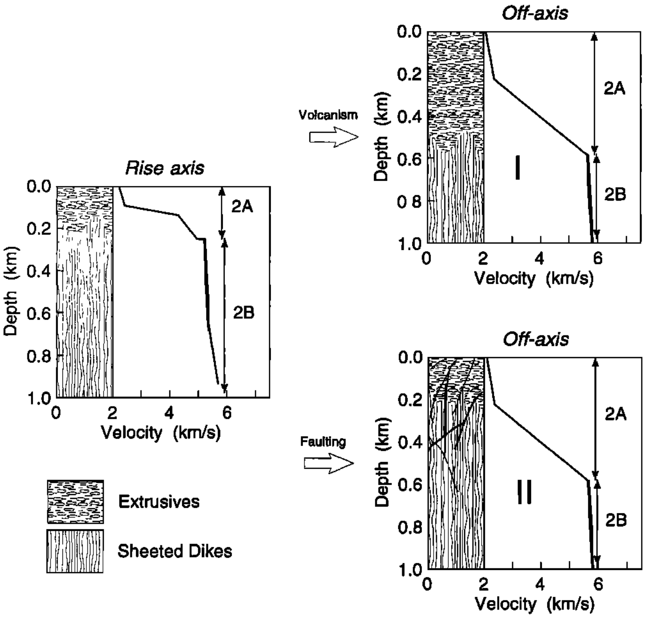

Figure 9. Two possible relationships between seismic and lithologic or porosity layering for crust created at fast spreading ridges. In case I, the major increase in seismic velocities at the base of layer 2A coincides with the region between the volcanic section and the sheeted dike complex. Therefore the thickening of layer 2A away from the neovolcanic zone would reflect an increase in the volcanic section. In case II the velocity gradient is the consequence of intense faulting as new crust moves away from the ridge crest. In this hypothesis the transition between layers 2A and 2B would not depend on the lithology. Modified from *Harding et al.* [1993].

In young oceanic crust (age ≤1–2 Ma), layer 2A is defined as a low-velocity section characterized by velocities in the range 2.2–2.8 km/s with a high-velocity gradient at its base [e.g., *Harding et al.*, 1989; *Cudrak and Clowes*, 1993; *Christeson et al.*, 1994; Hussenoeder et al., submitted manuscript, 2001]). The gradient at the layer 2A/2B transition (Figure 9) is presumably due to a reduction in cracking and porosity, but the underlying cause of this reduction is subject to debate: It could result from a transition in igneous rock type [e.g., *Harding et al.*, 1993] or it could be related to tectonically induced secondary cracking in layer 2A [e.g., *McClain et al.*, 1985]. The steep velocity increase creates high-energy reflections on multichannel seismic (MCS) profiles. By observing the symmetric deepening of this reflector away from the rise crest over a width corresponding to the neovolcanic zone, recent MCS experiments on young EPR crust suggested a model in which layer 2A corresponds to extrusives, while layer 2B is composed of sheeted dikes [*Harding et al.*, 1989, 1993; *Toomey et al.*, 1990; *Christeson et al.*, 1994]. In this interpretation the velocity gradient at the base of layer 2A would result from the increasing number of dikes with depth, while the thickening would be attributed to progressive burying of the sheeted dikes by volcanic eruptions as crust moves away from the rise axis (case I in Figure 9). *Hooft et al.* [1996] refined earlier stochastic studies [*Cann*, 1974] and proposed models of lava flow and dike emplacement that can reproduce the observed twofold to threefold thickening of layer 2A in the EPR accretion zone. Positive correlations between the thickness of the magnetic source layer and of seismic layer 2A have also been reported from the Endeavour segment of the northern Juan de Fuca Ridge [*Tivey and Johnson*, 1993], from the Cleft and Vance segments of the southern Juan de Fuca Ridge [*Tivey*, 1994] and from the 9°–10°N EPR segment [*Schouten et al.*, 1999]. Although many effects contribute to the oceanic magnetic field anomaly, the agreement between seismic measurements and the magnetic source layer lends support to the lithologic hypothesis for seismic layer 2A, at least within the neovolcanic zone.

Alternatively, the high-velocity (or porosity) gradient at the base of layer 2A may be the consequence of secondary processes. Intense fissuring, faulting, and geochemical alteration take place in the upper crust and modify its original porosity structure (porous extrusives on top of dense dikes). Indeed, hydrothermal circulation affects upper crustal seismic velocities by depositing minerals within the crack space and decreasing pore size [e.g., *Wilkens et al.*, 1991; *Wilcock et al.*, 1992; *Rohr*, 1994; *Grevemeyer et al.*, 1999]. In addition, as new crust moves away from the rise crest, the volcanic units become intensely fractured [*Karson*, 1998]. Faulting reduces the upper crustal velocities [*McClain et al.*, 1985], and such a process could cause a seismic signal similar to the deepening of layer 2A pseudoreflections documented by MCS surveys (case II in Figure 9). Most significant faulting occurs outside the neovolcanic zone [*Macdonald et al.*, 1996], so that the fracture hypothesis seems unable to explain the observed layer 2A thickening pattern near the ridge. Although this relationship between seismic layering and lithology may hold near the ridge, fissuring, faulting, and alteration undoubtedly modify the upper crust from its primary structure, and any initial relationship may not persist as the crust ages.

5.2. Insights From Layer 2A at the 9°03′N OSC

Our estimates of average layer 2A thickness (430 m) and surface velocity (2.9 km/s) are comparable to previous seismic analysis (510 m thickness [*Christeson et al.*, 1997] and 2.11–2.85 km/s [*Christeson et al.*, 1994] and 2.05–2.35 km/s [*Vera et al.*, 1990] velocities at 9°35′N). However, we observe much greater thickness variabilities than on the flanks of EPR midsegments where layer 2A varies from only 480 to 570 m at 14°15′S [*Kent et al.*, 1994] and from 360 to 500 m between 17°10′S and 17°40′S [*Carbotte et al.*, 1997]. Furthermore, the thickness of layer 2A (over 800 m) in the relict basins, the current overlap basin, and the propagating ridge tip is considerably greater than typical EPR crust. Thick areas occur in the western discordant zone and coincide with relict overlap basins 1a and 1b and less clearly with basin 3 (Figure 7). A recent wide-angle seismic line parallel to the rise axis and running through relict basin 3 confirms our assumption of thick layer 2A in this basin [*Canales et al.*, 1999]. Similar delays were documented previously in the crust affected by the migration of former OSCs on the flanks of the southern [*Bazin et al.*, 1998] and northern [*Christeson et al.*, 1997] EPR and of the Valu Fa Ridge [*Day et al.*, 2001]. Slower layer 2A velocities may be a potential explanation for these observations, however, Plate 3 clearly shows that increased thickness rather than lower velocities is responsible for the late layer 2A events in our study area.

Relict basin 2 is not associated with thick layer 2A nor with high magnetizations [*Carbotte and Macdonald*, 1992, Figure 4a]. We propose that these two observations are linked and may be explained by a different state of the axial discontinuity between 0.24 and 0.2 Ma. Indeed, kinematic modeling suggests that the offset of the OSC was reduced during this period and relict basin 2 was formed after a northward jump in opposition with the general migration trend [*Carbotte and Macdonald*, 1992]. In addition, the fact that the two areas of thick layer 2A are well separated in relict basins 1a and 1b would suggest that the two basins were not rafted simultaneously, as described in the alternative kinematic model of *Carbotte and Macdonald* [1992].

The complex kinematics of the OSC migration may generate highly irregular degree of fracturing in the upper crust, and the observed heterogeneity in layer 2A within the discordance zone could result from it. Furthermore, increasing faulting is observed along the 9°N segment toward the OSC [*Alexander and Macdonald*, 1996]. Our preferred interpretation, however, is that variable buildup of extrusives account for the layer 2A thickness pattern. Submersible measurements of extrusive thickness on seafloor outcrops support this hypothesis with variations of several hundreds of meters observed in complicated accretionary regimes such as Hess Deep [*Rivizzigno and Karson*, 1999]. An argument favoring the lithologic interpretation for seismic layer 2A comes from the distribution of faults and fissures in the area. A regional fault map derived from side-scan images [*Carbotte and Macdonald*, 1992, Figure 4c] clearly shows that present and relict overlap basins lack lineations, while the discordance zone on the eastern flank appears covered with fault scarps. At a smaller scale, deep-towed sonar studies reveal that the zone of thick layer 2A centered in the present overlap basin and propagating tip is not fissured [*Sempéré and Macdonald*, 1986]. The lack of fissuring may be only superficial, but the more inflated inside flank of the propagating tip cross section (cf. *Sempéré and Macdonald*, 1986, Plate 2) would suggest that the volcanic unit is simply thicker. In contrast with the highly fissured eastern ridge crest the overlap basin and the inside flank of the propagating limb are covered by small volcanic edifices which give them a hummocky surface, while the outside flank terrane appears even (Plate 6). Hummocky terrane is a common feature of many OSC basins [*Macdonald et al.*, 1992]. Only pillows are present in the thick layer 2A area on the eastern wall of the overlap basin, while sheet flows were observed elsewhere in the OSC region [*Sempéré and Macdonald*, 1986]. Pillows and small volcanic domes are not typical of EPR-type ridge crests at midsegments but are found in abundance at EPR segment ends [*White et al.*, 1999], in the median valley floor of the Mid-Atlantic Ridge, and in the Kilauea rift zone [*Smith and Cann*, 1999]. These observations would imply that the inside flank of the propagating limb is dominated by volcanism and spreading seems to be locked while the outside flank is dominated by extension and spreading. The eastern limb would act as a dam, and lavas would accumulate in the overlap basin. The buildup of extrusives at the propagating tip and in particular on its inside flank would then be generated by a long period of accumulation rather than by an increased magma budget at the tip. Indeed, there is no evidence for high magma budget at the propagating tip, as no magma lens is observed on the 3-D MCS data (the melt lens disappears where layer 2A thickness increases abruptly at 9°02′N, Plate 6) and as Fe-Ti basalts indicating small restricted magma bodies [*Sinton et al.*, 1983] were dredged at the tip. Alternatively, the dissimilarity between layer 2A growth on the eastern ridge and on the western one could result from accumulation of new extrusives on top of a preexisting layer as the eastern ridge propagates into old crust [*Carbotte et al.*, 2000]. This geometry, however, might not create the strong asymmetry observed between the two flanks of the propagating limb.

Layer 2A thickness is presumably related to the volcanic processes by which the extrusive layer is emplaced. Our analysis shows that layer 2A is more variable on the west than on the east flank of the axis; the layer is considerably thicker at the present propagating ridge tip than at the nonpropagating one. There appears to be a more general association between propagating rift tips and thicker layer 2A on axis. Six OSCs pres-

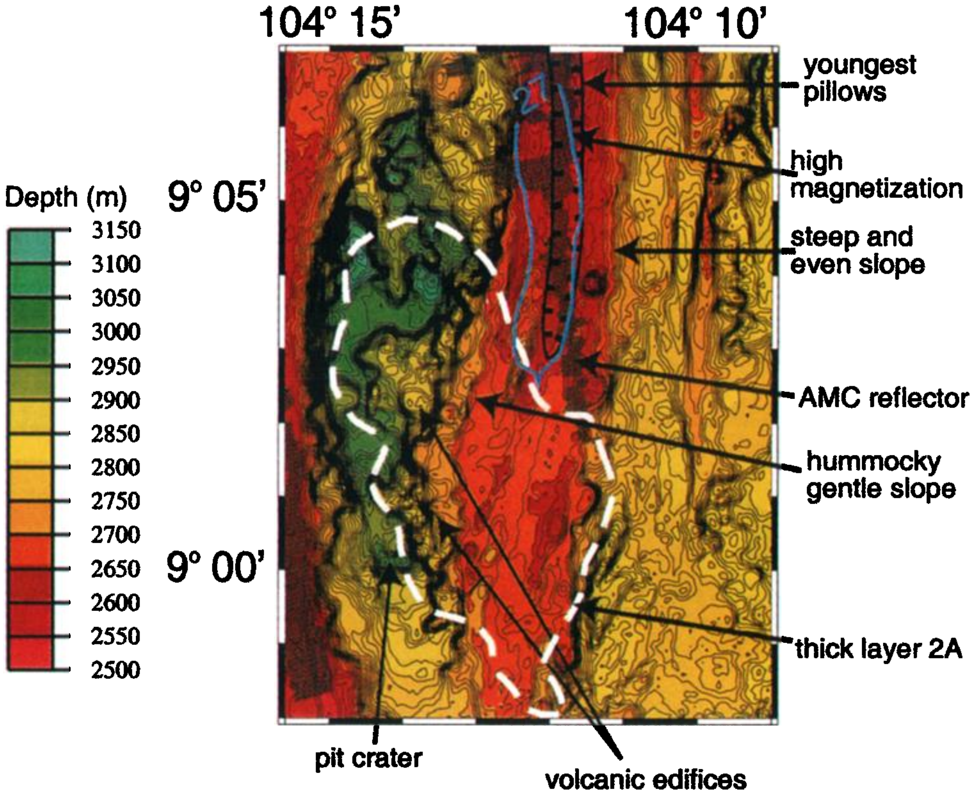

Plate 6. Thick layer 2A area with its geologic setting. The bathymetry map displays the asymmetric morphology of the eastern limb (50-m color interval and 12.5-m contour interval). Its outside flank appears smooth and slopes steeply toward the abyssal hill terrain, while the inside flank is covered with small volcanic edifices. The white dashed line shows the extent of a zone of thick seismic layer 2A extending between the overlap basin and the propagating limb. The shaded area shows the width of the axial magma chamber (AMC) reflector detected by a detailed 3-D MCS survey [*Kent et al.*, 2000]. The last 6 km of the melt sill plunges by 500 m to the south, which coincides with the gradual thickening of layer 2A. A band of young pillows mapped by side-scan images is confined within fissures that are presumably eruptive [*Sempéré and Macdonald*, 1986]. The narrow band of high magnetization intensity (magnetization corrected with source layer thickness) is contoured in blue (27 A/m).

ently offset the southern EPR; three of them at 15°55'S, 16°30'S, and 19°03'S are migrating away from the shallowest and most robust section of the EPR between 17°S and 17°30'S [*Cormier et al.*, 1996]. Interestingly, a 1991 along-axis seismic profile [*Hooft et al.*, 1997] indicates that these three OSCs show thicker seismic layer 2A at their propagating limbs than at the retreating ones. The three other OSCs at 17°55'S, 18°22'S, and 18°36'S present no evidence of migration [*Cormier and Macdonald*, 1994] nor are they associated with a thicker layer 2A on one of their ridge tips. A detailed analysis would be necessary before generalizing this correlation between layer 2A thickness and OSC migrations. In particular, because the 1991 seismic survey did not follow both ridge limbs at OSCs, it is possible that the apparent deepening of the layer 2A reflector toward the discontinuities results, to some extent, from the drifting of the ship track away from the rise crest.

5.3. High Axial Magnetization

There are a multiplicity of factors that contribute to the magnetization intensity of the basalts including paleointensity fluctuations, basalt geochemistry, alteration processes, and titanomagnetite grain size effects. Although these effects are difficult to separate, a few pertinent observations can be made about the magnetization distribution at the OSC area. *Gee and Kent* [1997, 1998] have demonstrated that high iron contents are usually accompanied by high proportions of titanomagnetite and increased natural remanent magnetization (NRM) in lavas. In this area the high-amplitude magnetic anomaly at the ridge tip has been previously attributed entirely to Fe-rich basalts [*Sempéré et al.*, 1988]. This interpretation was supported by samples dredged from the eastern ridge which have higher FeO* content (total iron as FeO) than those from the western tip [*Natland et al.*, 1986; *Langmuir*, 1988; *Tighe et al.*, 1988; *Sempéré et al.*, 1988; *Sempéré*, 1991]. Fe-Ti basalts are often found near propagating rifts, and it has been proposed that these highly fractionated lavas erupt from isolated magma chambers [*Sinton et al.*, 1983]. The complex geometry of the eastern ridge AMC is now well resolved: the width of the melt sill narrows considerably southward, while it deepens and appears to be fed, at least partially, by discrete conduits of melt ascending from beneath the overlap basin [*Kent et al.*, 2000]. Although continuous, the tortuous geometry of the melt sill may inhibit magma mixing, and Fe-rich lavas may be generated by fractional crystallization. It is interesting to notice that Fe-rich lavas and a thick extrusive layer are coincident at the propagating limb, and we infer that both make a positive contribution to the magnetic anomaly. As suggested by *Lee et al.*

[1996], these two factors could be linked: A deep magma chamber is more likely to erupt evolved lavas enriched in iron and titanium, while thick extrusives may simply increase the depth of magma chamber below the seafloor level. Whether the deepening of the magma chamber and the thickening of the extrusive layer toward the south end of the propagating ridge tip are really related is unclear and beyond the scope of this study. The general depth of the magma lens is probably controlled by the thermal structure of the ridge axis [*Phipps Morgan and Chen*, 1993]. The thickness of the extrusives, however, is controlled by the pressure on the melt lens, which is a function of its depth and the overlying rock densities. *Buck et al.* [1997] predict that thicker low-density extrusives can pile up on ridges with a deeper melt lens, and our observations along the propagating ridge provide new support for their model.

The broad high-amplitude magnetization intensity calculated at the propagating limb (Plate 5e) is undoubtedly related to the Fe-rich basalts, but Fe enrichment may not account for the entire total intensity variation. According to the empirical relationship of *Gee and Kent* [1998] a factor of 4.44 A/m per %FeO* (reduced to an equatorial reference frame) is observed between FeO* content of sampled glass and NRM intensities. The maximum variability measured in FeO* contents at the OSC is 5.2% (FeO* varies from 8.6 to 13.8% [*Langmuir*, 1988; *Tighe et al.*, 1988; *Natland et al.*, 1986]). If the paleointensity were similar to today at 9°03′N latitude, the empirical relationship predicts that an intensity range of 5.2% in iron enrichment would generate a NRM variability of only 24 A/m within the samples. A careful study of the magnetic properties of basalts dredged within the OSC basin, from the west flank of the OSC, and on the eastern limb shows that average NRM is greatest for the samples collected on the eastern limb (50.4 ± 15.3 A/m on the eastern limb versus 33.5 ± 18.6 A/m in the basin and 17.6 ± 6.9 and 8.4 ± 2.4 A/m on the west flank [*Sempéré et al.*, 1988]). The entire NRM range measured in these samples is 71.7 A/m [*Sempéré et al.*, 1988, Table IV] which is much greater than what the Fe enrichment alone would predict. We therefore speculate that the samples may also carry an important paleointensity signal and that the narrow band of remaining high magnetization (Plate 5e) may be related to variations in paleointensity.

Changes in the Earth's magnetic field can account for large variations in magnetization [*Merrill et al.*, 1996; *Gee et al.*, 2000]. On the basis of sea surface magnetic data, *Gee et al.* [1996] suggest that field intensity fluctuations are the main cause for the central anomaly magnetic high signal (CAMH) widely observed at mid-ocean ridges. Absolute paleointensity determinations of the dipole moment recorded in archeomagnetic and volcanic materials show intense and rapid fluctuations in Earth's magnetic field since 40 ka: The dipole moment now at 7.9×10^{22} A m^2, peaked to near 11×10^{22} A m^2 at 1–3 ka but was as low as 2.75×10^{22} A m^2 near 40–50 ka [*Merrill et al.*, 1996]. We suggest that the high magnetization intensity centered on the eastern ridge crest (Plate 5e) could be related to lavas erupted during the peak dipole intensity. This narrow band coincides with the occurrence of the youngest pillow basalts observed on near-bottom photographs (relative age of 1.2–2.2 on a 1–4 scale inferred from sediment cover and from fine-scale characteristics [*Sempéré and Macdonald*, 1986] (Plate 6)). Additional factors such as low temperature oxidation [*Klitgord*, 1976; *Schouten et al.*, 1999] and magnetic grain size [*Prévot et al.*, 1979] as well as potential reheating and deformation [*Carbotte and Macdonald*, 1992] within the magnetized crust must exist in the magnetization intensity map, but the present data cannot isolate such complex contributions.

Recent magnetic models using seismically constrained layer 2A thicknesses have successfully recovered the short-wavelength signal of the CAMH on the Juan de Fuca ridge [*Tivey and Johnson*, 1993; *Tivey*, 1994] and on the northern EPR [*Schouten et al.*, 1999] using a rapide decrease of rock magnetization with age. These near-bottom magnetic studies support the hypothesis that seismic layer 2A roughly corresponds to the magnetized extrusive layer and, consequently, has a lithologic origin. We speculate that in addition to the layer thickness variations a significant part of the magnetic signal is generated by paleofield intensity and geochemical variations such as Fe enrichment. However, a more complete and detailed magnetic survey combined with dredges and cores would be necessary to uncover fully the interplay between the magnetic signature and the seismic signal observed at this OSC.

6. Conclusions

Seismic models of the upper crust for different accretion environments can provide important insight into the accretionary process and can help discriminate between the various geological interpretations of layer 2A. This study at an OSC brings a valuable addition to the more extensive seismic studies already completed on midsegments along the EPR. First-arrival layer 2A travel times indicate a very heterogeneous upper crustal structure in the area of the 9°03′N OSC: We observe significant travel time delays (up to 0.3 s variations in integrated travel times through the upper 1.5 km of crust). We interpret these delays as primarily due to variability in layer 2A thickness, but we cannot entirely discard lower layer 2A velocities due to intense fracturing as an alternative explanation.

The along-axis migration of the 9°03′N OSC has resulted in an off-axis V-shaped discordance zone. A seismic velocity signature is imprinted in the crust of this discordant region. Areas of thick layer 2A are found on the Pacific plate within relict basins. In contrast, the upper crustal structure of the Cocos plate appears more uniform. We suggest that thick layer 2A is a typical signature of accumulation of lavas in overlap basins.

The present propagating limb, the eastern spreading ridge, appears asymmetric in its structure and morphology and seems to protrude into the overlap basin. Its inside slope is covered with small secondary volcanic edifices that coincide with a zone of thick layer 2A, while the outside slope is steep, with a smooth terrane and normal layer 2A thickness. We infer that the inside flank is locked while the outside one drifts away, resulting in an asymmetric layer 2A growth.

Our reinterpretation of the surface magnetic data suggests that a substantial portion of the high magnetization observed at the propagating ridge tip is related to magnetic source layer thickness variation rather than solely to Fe-rich basalts as previously proposed. The contribution of geomagnetic field intensity variations may also be significant, and we propose that the confined band of fresh pillows detected by previous deep-towed imagery [*Sempéré and Macdonald*, 1986] contributes to a narrow magnetization high centered on the northern half of the propagating limb. Our results are limited, however, by the fact that only surface magnetic measurements are available for the OSC area.

Appendix A

A1. Ocean Bottom Data Collection

The on-bottom array consisted a combination of hydrophones and seismometers (Figure 1). Scripps Low-Cost Hardware for Earth Applications and Physical Oceanography (L-Cheapo) hydrophones operated with a sampling frequency of 250 Hz, while Cambridge mini-DOBS hydrophones operated with a sampling frequency of 128 Hz. Detailed descriptions of the L-Cheapo package are given by *Constable et al.* [1998] (and are available at http://www.obsip.org).

A2. Clock Drift Correction

The clock drift correction is important to travel time inversion methods which compare arrivals from a common set of shots to multiple ocean bottom instruments. The L-Cheapo clock drift rates were estimated from predeployment and postdeployment measurements. They ranged from 0.25 to 5.65 ms/d. Results of laboratory tests ensure that the drifts are linear even in cold environments and accurate corrections can be made through linear interpolation. The mini-DOBS clocks were corrected primarily using interpolation, checked against water wave arrival times. For our travel time inversions we only used the mini-DOBS that showed linear drifts.

A3. Bathymetric Correction

Accurate bathymetry is desirable for marine refraction processing since the topographic signal dominates the variations in travel times. The bathymetry used in this study is a compilation of the new Hydrosweep data collected during the ARAD cruise with old grids. Prior data including SeaMARC II and Sea Beam data gathered between 1987 and 1990 were available in a mosaic grid [*Macdonald et al.*, 1992]. Because of the merging of the different data formats and poor navigation at the time the precision of the existing chart was not adequate for our detailed seismic analysis. We found location discrepancies between the old chart and the new data up to 1 min (1.8 km). Within our model area the coverage of the new bathymetric data is nearly complete (~80% of our model box) with data gaps being filled with the old chart.

A4. Instrument Relocation

Shipboard navigation and streamer positioning were achieved through an INMARSAT-based Differential Global Positioning System, which was accurate to within a few meters. We solved for ocean bottom instrument coordinates and depths by inverting travel times of direct water wave arrivals. The shot positions were derived from ship heading and position, and the geometry of the air gun array. Initial drop locations were taken from GPS navigation, and the initial instrument depths were derived by interpolating the bathymetry grid at the drop locations.

A.4.1. L-Cheapos. We used shots located within a radius of 5 km of the instrument. Travel times through the water column were calculated using a weighted average velocity value estimated from conductivity-temperature-depth (CTD) profiles. We assumed that the deflection of the ray path from a straight line was negligible for such short ranges. New instrument depths and locations were estimated by a least squares fit of the water wave travel times. The average difference between the inverted depths and the seafloor depths is 6 m, and the final RMS travel time residuals are 2 to 7 ms (sample interval of 4 ms). Instruments experienced lateral drifts varying from 65 to 266 m during descent.

A.4.2. Mini-DOBSs. The RMS travel time residuals for instrument relocations were estimated using a complete CTD profile and were between 6 and 12 ms (sample interval of 8 ms) [Tong et al., manuscript in preparation, 2001).

A5. Data Quality

The average total data recovery for the ocean bottom array is 79% (100% for the L-Cheapos), and the data quality is generally good for the two instrument designs. Picking the first arrivals from the seismic traces is accurate to within 4–24 ms (average picking error is ~12 ms). We manually picked *P* wave arrivals from the hydrophone data as automatic picking is potentially error prone in rough topography.

Acknowledgments. We thank the captain and the crew of the R/V *Maurice Ewing* and all members of the scientific party for the success of cruise EW9707. We also thank Paul Henkart for supplying SIOSEIS seismic processing package and Jeff Gee for his aid with the magnetic processing. Gail Christeson, Suzanne Carbotte, and Maurice Tivey provided careful reviews that improved the manuscript. The ARAD seismic experiment is a collaboration between the Scripps Institution of Oceanography and the University of Cambridge. This work was supported by the National Science Fundation grant OCE96-1330 to the Scripps Institution of Oceanography.

References

Alexander, R. T., and K. C. Macdonald, Sea Beam, SeaMARK II and *Alvin*-based studies of faulting on the East Pacific Rise 9°20′–9°50′N, *Mar. Geophys. Res.*, *18*, 557–587, 1996.

Barclay, A. H., D. R. Toomey, and S. C. Solomon, Seismic structure and crustal magmatism at the Mid-Atlantic Ridge, 35°N, *J. Geophys. Res.*, *103*, 17,827–17,844, 1998.

Batiza, R., and S. H. Margolis, A model for the origin of small nonoverlapping offsets (SNOOs) of the East Pacific Rise, *Nature*, *320*, 439–441, 1986.

Bazin, S., Three-dimensional crustal structure of East Pacific Rise discontinuities from tomographic inversions, Ph.D. thesis, Univ. of Calif., San Diego, 2000.

Bazin, S., H. van Avendonk, A. J. Harding, J. A. Orcutt, J. P. Canales, R. S. Detrick, and MELT Group, Crustal structure of the flanks of the East Pacific Rise: Implications for overlapping spreading centers, *Geophys. Res. Lett.*, *25*, 2213–2216, 1998.

Blakely, R. J., *Potential Theory in Gravity and Magnetic Applications*, 441 pp., Cambridge Univ. Press, New York, 1995.

Buck, W. R., S. M. Carbotte, and C. Mutter, Controls on extrusion at mid-ocean ridges, *Geology*, *25*, 935–938, 1997.

Canales, J. P., R. S. Detrick, D. R. Toomey, and W. S. D. Wilcock, Variations in crustal thickness and *P*-wave velocity along the East Pacific Rise between the Clipperton and Siqueiros transforms from wide-angle seismic data, *Eos Trans. AGU*, *80*(46), Fall Meet. Suppl., F995, 1999.

Cann, J. R., A model for oceanic crustal structure developed, *Geophys. J. R. Astron. Soc.*, *39*, 169–187, 1974.

Carbotte, S., and K. Macdonald, East Pacific Rise 8°–10°30′N: Evolution of ridge segments and discontinuities from SeaMARC II and three-dimensional magnetic studies, *J. Geophys. Res.*, *97*, 6959–6982, 1992.

Carbotte, S., J. C. Mutter, and L. Xu, Contribution of volcanism and tectonism to axial and flank morphology of the southern East Pacific Rise, 17°10′–17°40′S, from a study of layer 2A geometry, *J. Geophys. Res.*, *102*, 10,165–10,184, 1997.

Carbotte, S., A. Solomon, and G. Ponce-Correa, Evaluation of morphological indicators of magma supply and segmentation from a seismic reflection study of the East Pacific Rise 15°30′–17°N, *J. Geophys. Res.*, *105*, 2737–2759, 2000.

Červený, V., I. A. Molotkov, and I. Psencik, *Ray Method in Seismology*, Charles Univ. Press, Prague, 1977.

Christensen, N. I., Ophiolites, seismic velocities and oceanic crustal structure, *Tectonophysics*, *47*, 131–157, 1978.

Christensen, N. I., and M. H. Salisbury, Structure and constitution of the lower oceanic crust, *Rev. Geophys.*, *13*, 57–86, 1975.

Christeson, G. L., G. M. Purdy, and G. J. Fryer, Seismic constraints on shallow crustal emplacement processes at the fast spreading East Pacific Rise, *J. Geophys. Res.*, *99*, 17,957–17,973, 1994.

Christeson, G. L., P. R. Shaw, and J. D. Garmany, Shear and compressional wave structure of the East Pacific Rise, 9°–10°N East Pacific Rise, *J. Geophys. Res.*, *102*, 7821–7835, 1997.

Constable, S. C., A. S. Orange, G. M. Hoversten, and H. F. Morrison, Marine magnetotellurics for petroleum exploration, part 1, A seafloor equipment system, *Geophysics*, *63*, 816–825, 1998.

Cormier, M.-H., and K. C. Macdonald, East Pacific Rise 1°8–19°S: Asymmetric spreading and ridge reorientation by ultrafast migration of axial discontinuities, *J. Geophys. Res.*, *99*, 543–564, 1994.

Cormier, M.-H., D. S. Scheirer, and K. C. Macdonald, Evolution of the East Pacific Rise at 16°–19°S since 5 Ma: Bisection of overlapping spreading centers by new, rapidly propagating ridge segments, *Mar. Geophys. Res.*, *18*, 53–84, 1996.

Cudrak, C. F., and R. M. Clowes, Crustal structure of Endeavour ridge segment, Juan de Fuca Ridge, from a detailed seismic refraction survey, *J. Geophys. Res.*, *98*, 6329–6349, 1993.

Day, A. J., C. Peirce, and M. C. Sinha, Three-dimensional crustal structure and magma chamber geometry at the intermediate-spreading, back-arc Valu Fa Ridge, Lau Basin—results of a wide-angle seismic tomographic inversion, *Geophys. J. Int.*, in press, 2001.

Detrick, R., J. Collins, R. Stephen, and S. Swift, In situ evidence for the nature of the seismic layer 2/3 boundary in oceanic crust, *Nature*, *370*, 288–290, 1994.

Fornari, D. J., R. M. Haymon, M. R. Perfit, T. K. P. Gregg, and M. H. Edwards, Axial summit trough of the East Pacific Rise 9°–10°N: Geological characteristics and evolution of the axial zone on fast spreading mid-ocean ridges, *J. Geophys. Res.*, *103*, 9827–9855, 1998.

Francheteau, J., R. Armijo, J. L. Cheminee, R. Hekinian, P. Lonsdale, and N. Blum, Dyke complex of the East Pacific Rise exposed in the walls of Hess Deep and structure of the upper oceanic crust, *Earth Planet. Sci. Lett.*, *111*, 109–121, 1992.

Gee, J., and D. V. Kent, Magnetization of axial lavas from the southern East Pacific Rise (14°–23°S): geochemical controls on magnetic properties, *J. Geophys. Res.*, *102*, 24,873–24,886, 1997.

Gee, J., and D. V. Kent, Magnetic telechemistry and magmatic segmentation on the southern East Pacific Rise, *Earth Planet. Sci. Lett.*, *164*, 379–386, 1998.

Gee, J., D. A. Schneider, and D. V. Kent, Marine magnetic anomalies as recorders of geomagnetic intensity variations, *Earth Planet. Sci. Lett.*, *144*, 327–335, 1996.

Gee, J., S. C. Cande, J. A. Hildebrand, K. Donnelly, and R. L. Parker, Geomagnetic intensity variations over the past 780 kyr obtained from near-seafloor magnetic anomalies, *Nature*, *408*, 827–832, 2000.

Grevemeyer, I., N. Kaul, H. Villinger, and W. Weigel, Hydrothermal activity and the evolution of the seismic properties of upper oceanic crust, *J. Geophys. Res.*, *104*, 5069–5079, 1999.

Gripp, A. E., and R. G. Gordon, Current plate velocities relative to the hotspots incorporating the NUVEL-1 global plate motion model, *Geophys. Res. Lett.*, *17*, 1109–1112, 1990.

Harding, A. J., M. E. Kappus, J. A. Orcutt, E. E. Vera, P. Buhl, J. C. Mutter, R. Detrick, and T. Brocher, The structure of young oceanic crust at 13°N on the East Pacific Rise from expanding spread profiles, *J. Geophys. Res.*, *94*, 12,163–12,196, 1989.

Harding, A. J., G. M. Kent, and J. A. Orcutt, A multichannel seismic investigation of upper crustal structure at 9°N on the East Pacific Rise: Implications for crustal accretion, *J. Geophys. Res.*, *98*, 13,925–13,944, 1993.

Haymon, R. M., D. J. Fornari, M. Edwards, S. M. Carbotte, D. Wright, and K. C. Macdonald, Hydrothermal vent distribution along the East Pacific Rise crest (latitude 9°09′–54′N) and its relationship to magmatic and tectonic processes on fast spreading mid-ocean ridges, *Earth Planet. Sci. Lett.*, *104*, 513–534, 1991.

Hooft, E. E. E., H. Schouten, and R. S. Detrick, Constraining crustal emplacement processes from the variation in seismic layer 2A thickness at the East Pacific Rise, *Earth Planet. Sci. Lett.*, *142*, 289–307, 1996.

Hooft, E. E. E., R. S. Detrick, and G. M. Kent, Seismic structure and indicators of magma budget along the southern East Pacific Rise, *J. Geophys. Res.*, *102*, 27,341–27,354, 1997.

Houtz, R., and J. Ewing, Upper crustal structure as a function of plate age, *J. Geophys. Res.*, *81*, 2490–2498, 1976.

Karson, J. A., Internal structure of oceanic lithosphere: a perspective from tectonic windows, in *Faulting and Magmatism at Mid-ocean Ridges*, *Geophys. Monogr. Ser.*, vol. 106, edited by W. R. Buck et al., pp. 177–218, AGU, Washington, D. C., 1998.

Kennett, B. L. N., and J. A. Orcutt, A comparison of travel time inversions for marine refraction profiles, *J. Geophys. Res.*, *81*, 4061–4070, 1976.

Kent, G. M., A. J. Harding, J. A. Orcutt, R. S. Detrick, J. C. Mutter, and P. Buhl, Uniform accretion of oceanic crust south of the Garrett transform at 14°15′S on the East Pacific Rise, *J. Geophys. Res.*, *99*, 9097–9116, 1994.

Kent, G. M., et al., Evidence from three-dimensional seismic reflectivity images for enhanced melt supply beneath mid-ocean-ridge discontinuities, *Nature*, *406*, 614–618, 2000.

Klitgord, K. D., Sea-floor spreading: the central anomaly high, *Earth Planet. Sci. Lett.*, *29*, 201–209, 1976.

Langmuir, C. H., Petrology data base, in *East Pacific Rise Data Synthesis: Final Report*, vols. II and III, edited by S. Tighe, Joint Oceanogr. Inst. Inc., Washington, D. C., 1988.

Langmuir, C. H., J. F. Bender, and R. Batiza, Petrological and tectonic segmentation of the East Pacific Rise, 5°30′–14°30′N, *Nature*, *322*, 422–429, 1986.

Lee, S.-M., S. C. Solomon, and M. A. Tivey, Fine-scale crustal magnetization variations and segmentation of the East Pacific Rise, 9°10′–9°50′N, *J. Geophys. Res.*, *101*, 22,033–22,050, 1996.

Lonsdale, P., Overlapping rift zones at the 5.5°S offset of the East Pacific Rise, *J. Geophys. Res.*, *88*, 9393–9406, 1983.

Lonsdale, P., Nontransform offsets of the Pacific-Cocos plate boundary and their traces on the rise flank, *Geol. Soc. Am. Bull.*, *96*, 313–327, 1985.

Macdonald, K. C., S. P. Miller, S. P. Huestis, and F. N. Spiess, Three-dimensional modeling of a magnetic reversal boundary from inversion of deep-tow measurements, *J. Geophys. Res.*, *85*, 3670–3680, 1980.

Macdonald, K. C., et al., The East Pacific Rise and its flanks 8°–18°N: History of segmentation, propagation and spreading direction based on SeaMARK II and Sea Beam studies, *Mar. Geophys. Res.*, *14*, 299–344, 1992.

Macdonald, K. C., P. J. Fox, R. T. Alexander, R. Pockalny, and P. Gente, Volcanic growth faults and the origin of Pacific abyssal hills, *Nature*, *380*, 125–129, 1996.

McClain, J. S., J. A. Orcutt, and M. Burnett, The East Pacific Rise in cross section: A seismic model, *J. Geophys. Res.*, *90*, 8627–8639, 1985.

McDonald, M. A., S. C. Webb, J. A. Hildebrand, B. D. Cornuelle, and C. G. Fox, Seismic structure and anisotropy of the Juan de Fuca Ridge at 45°N, *J. Geophys. Res.*, *99*, 4857–4873, 1994.

Merrill, R. T., M. W. McElhinny, and P. L. McFadden, *The Magnetic Field of the Earth; Paleomagnetism, the Core, and the Deep Mantle*, *Int. Geophys. Ser.*, vol. 63, 531 pp., Academic, San Diego, Calif., 1996.

Moser, T. J., Shortest path calculation of rays, *Geophysics*, *56*, 59–67, 1991.

Moser, T. J., G. Nolet, and R. Snieder, Ray bending revisited, *Bull. Seismol. Soc. Am.*, *82*, 259–288, 1992.

Natland, J., C. Langmuir, J. Bender, R. Batiza, and C. Hopson, Petrologic systematics in the vicinity of the 9°N non-transform offset, East Pacific Rise, *Eos Trans. AGU*, *67*, 1254, 1986.

Nicolas, A., *Structure of Ophiolites and Dynamics of Oceanic Lithosphere*, *Petrol. Struct. Geol.*, vol. 4, 367 pp., Kluwer Acad., Norwell, Mass., 1989.

Parker, R. L., and S. P. Huestis, The inversion of magnetic anomalies in the presence of topography, *J. Geophys. Res.*, *79*, 1587–1593, 1974.

Phipps Morgan, J., and Y. J. Chen, Dependence of ridge-axis morphology on magma supply and spreading rate, *Nature*, *364*, 706–708, 1993.

Phipps Morgan, J., A. J. Harding, G. M. Kent, J. A. Orcutt, and Y. J. Chen, An observational and theoretical synthesis of magma chamber geometry and crustal genesis along a mid-ocean ridge spreading center, in *Magmatic Systems*, edited by M. P. Ryan, pp. 139–178, Academic, San Diego, Calif., 1994.

Prévot, M., A. Lecaille, and R. Hekinian, Magnetism of the Mid-Atlantic Ridge crest near 37°N from FAMOUS and DSDP results: A review, in *Deep Drilling Results in the Atlantic Ocean: Ocean crust*, *Maurice Ewing Ser.*, vol. 2, edited by M. Talwani, C. G. Harrison, and D. E. Hayes, pp. 210–229, AGU, Washington, D. C., 1979.

Raitt, R. W., The crustal rocks, in *The Sea*, vol. 3, *The Earth Beneath the Sea*, edited by M. N. Hill, pp. 85–102, Wiley-Interscience, New York, 1963.

Rivizzigno, P. A., and J. A. Karson, Temporal variations in relative thickness of the extrusive and sheeted dike units in EPR crust exposed at Hess Deep Rift: Implications for models of upper crustal construction, *Eos Trans. AGU*, *80*(46), Fall Meet. Suppl., F984, 1999.

Rohr, K. M. M., Increase of seismic velocities in upper oceanic crust and hydrothermal circulation in the Juan de Fuca plate, *Geophys. Res. Lett.*, *21*, 2163–2166, 1994.

Rohr, K. M. M., B. Milkereit, and C. J. Yorath, Asymmetric deep crustal structure across the Juan de Fuca Ridge, *Geology*, *16*, 533–537, 1988.

Schouten, H., M. A. Tivey, D. J. Fornari, and J. R. Cochran, Central anomaly magnetization high: Constraints on the volcanic construction and architecture of seismic layer 2A at a fast-spreading mid-ocean ridge, EPR at 9°30′–50′N, *Earth Planet. Sci. Lett.*, *169*, 37–50, 1999.

Sempéré, J. C., High-magnetization zones near spreading center discontinuities, *Earth Planet. Sci. Lett.*, *107*, 389–405, 1991.

Sempéré, J.-C., and K. C. Macdonald, Deep-Tow studies of the overlapping spreading centers at 9°03′N on the East Pacific Rise, *Tectonics*, *5*, 881–900, 1986.

Sempéré, J.-C., K. C. Macdonald, and S. P. Miller, Overlapping spreading centers: 3-D inversion of the magnetic field at 9°03′N on the East Pacific Rise, *Geophys. J. R. Astron. Soc.*, *79*, 799–811, 1984.

Sempéré, J.-C., A. Meshkov, M. Thommeret, and K. C. Macdonald, Magnetic properties of some young basalts from the East Pacific Rise, *Mar. Geophys. Res.*, *9*, 131–146, 1988.

Sinton, J. M., D. S. Wilson, D. M. Christie, R. N. Hey, and J. T. Delaney, Petrologic consequences of rift propagation on oceanic spreading centers, *Earth Planet. Sci. Lett.*, *62*, 193–207, 1983.

Smallwood, J. R., and R. S. White, Crustal accretion at the Reykjanes Ridge, 61°–62°N, *J. Geophys. Res.*, *103*, 5185–5201, 1998.

Smith, D. K., and J. R. Cann, Constructing the upper crust of the Mid-Atlantic Ridge: A reinterpretation based on the Puna Ridge, Kilauea volcano, *J. Geophys. Res.*, *104*, 25,379–25,399, 1999.

Sohn, R. A., S. C. Webb, J. A. Hildebrand, and B. D. Cornuelle, Three-dimensional tomographic velocity structure of upper crust, CoAxial segment, Juan de Fuca Ridge: Implications for on-axis evolution and hydrothermal circulation, *J. Geophys. Res.*, *102*, 17,670–17,695, 1997.

Spudich, P., and J. A. Orcutt, Petrology and porosity of an oceanic crust site: results from wave form modeling of seismic refraction data, *J. Geophys. Res.*, *85*, 1409–1433, 1980.

Talwani, M., C. C. Windisch, and M. G. Langseth Jr., Reykjanes Ridge crest: A detailed geophysical study, *J. Geophys. Res.*, *76*, 473–517, 1971.

Tighe, S. A., R. S. Detrick, P. J. Fox, C. H. Mutter, W. B. Ryan, and R. C. Tyce, Petrology data base, in *East Pacific Rise Data Synthesis: Final Report*, vol. I, edited by S. Tighe, Joint Oceanogr. Instit. Inc., Washington, D. C., 1988.

Tivey, M. A., Fine-scale magnetic anomaly field over the southern Juan de Fuca Ridge: Axial magnetization low and implications for crustal structure, *J. Geophys. Res.*, *99*, 4833–4855, 1994.

Tivey, M. A., and H. P. Johnson, Variations in oceanic crustal structure and implications for the fine-scale magnetic anomaly signal, *Geophys. Res. Lett.*, *20*, 1879–1882, 1993.

Toomey, D. R., G. M. Purdy, S. C. Solomon, and W. S. D. Wilcock, The three-dimensional seismic velocity structure of the East Pacific Rise near latitude 9°30′N, *Nature*, *347*, 639–645, 1990.

Toomey, D. R., S. C. Solomon, and G. M. Purdy, Tomographic imaging of the shallow crustal structure of the East Pacific Rise at 9°30′N, *J. Geophys. Res.*, *99*, 24,135–24,157, 1994.

Van Avendonk, H., An investigation of the crustal structure of the Clipperton transform fault area using 3-D seismic tomography, Ph.D. thesis, 249 pp., Univ. of Calif., San Diego, 1998.

Van Avendonk, H. J. A., A. J. Harding, J. A. Orcutt, and J. S. McClain, A two-dimensional tomographic study of the Clipperton transform fault, *J. Geophys. Res.*, *103*, 17,885–17,899, 1998.

Van Avendonk, H. J. A., A. J. Harding, J. A. Orcutt, and W. S. Holbrook, Hybrid shortest path and ray-bending method for traveltime and raypath calculations, *Geophysics*, in press, 2001.

Vera, E. E., J. C. Mutter, P. Buhl, J. A. Orcutt, A. J. Harding, M. E. Kappus, R. S. Detrick, and T. M. Brocher, The structure of 0- to 0.2-m.y.-old oceanic crust at 9°N on the East Pacific Rise from expanding spread profiles, *J. Geophys. Res.*, *95*, 15,529–15,556, 1990.

White, S. M., K. C. Macdonald, R. Haymon, and J. Sinton, Volcanic segmentation of the SEPR revealed by regional along-strike changes in lava morphology, *Eos Trans. AGU*, *80*(46), Fall Meet. Suppl., F1097, 1999.

Wilcock, W. S. D., S. C. Solomon, G. M. Purdy, and D. R. Toomey, The seismic attenuation structure of a fast-spreading mid-ocean ridge, *Science*, *258*, 1470–1474, 1992.

Wilkens, R. H., G. J. Fryer, and J. Karsten, Evolution of porosity and seismic structure of upper oceanic crust: Importance of aspect ratios, *J. Geophys. Res.*, *96*, 17,981–17,995, 1991.

Zhang, J., and M. N. Toksöz, Nonlinear refraction traveltime tomography, *Geophysics*, *63*, 1726–1737, 1998.

P. J. Barton, R. W. Hobbs, J. W. Pye, C. H. Tong, and R. S. White, Bullard Laboratories, Department of Earth Sciences, University of Cambridge, Madingley Road, Cambridge CB3 0EZ, England, UK. (barton@esc.cam.ac.uk; rwhite@esc.cam.ac.uk)

S. Bazin and S. C. Singh, Laboratoire de Géosciences Marines, Institut de Physique du Globe de Paris, 4 place Jussieu, Tour 14, case 89, F-75252 Paris cedex 05, France. (bazin@ipgp.jussieu.fr; singh@ipgp.jussieu.fr)

A. J. Harding, G. M. Kent, and J. A. Orcutt, Cecil H. and Ida M. Green Institute of Geophysics and Planetary Physics, Scripps Institution of Oceanography, University of California, San Diego, 9500 Gilman Drive, La Jolla, CA 92903. (harding@eos.ucsd.edu; gkent@eos.ucsd.edu; jorcutt@igpp.ucsd.edu)

M. C. Sinha, Oceanography Center, School of Ocean and Earth Science, University of Southampton, European Way, Southampton SO14 3ZH, England, UK. (Martin.Sinha@soc.soton.ac.uk)

H. J. A. Van Avendonk, Department of Geology and Geophysics, University of Wyoming, P.O. Box 3006, 16th and Gibbon Street, Laramie, WY 82071. (harm@uwyo.edu)

(Received July 6, 2000; revised January 30, 2001;
accepted February 14, 2001.)